Key Points:
- Reactive transport model of secondary water quality impacts from crude oil spill
- Distinct oil constituent properties drive secondary plume production
- Direct CH_4 and CO_2 outgassing and Fe sorption decrease secondary plumes

Correspondence to:
G.-H. C. Ng,
gcng@umn.edu

Reactive transport modeling of geochemical controls on secondary water quality impacts at a crude oil spill site near Bemidji, MN

Gene-Hua Crystal Ng[1,2], Barbara A. Bekins[2], Isabelle M. Cozzarelli[3], Mary Jo Baedecker[3], Philip C. Bennett[4], Richard T. Amos[5], and William N. Herkelrath[2]

[1]Deptartment of Earth Sciences, University of Minnesota, Minneapolis, Minnesota, USA, [2]U.S. Geological Survey, Menlo Park, California, USA, [3]U.S. Geological Survey, Reston, Virgina, USA, [4]Deptartment of Geological Sciences, University of Texas at Austin, Austin, Texas, USA, [5]Deptartment of Earth Sciences, Carleton University, Ottawa, Ontario, Canada

Abstract Anaerobic biodegradation of organic amendments and contaminants in aquifers can trigger secondary water quality impacts that impair groundwater resources. Reactive transport models help elucidate how diverse geochemical reactions control the spatiotemporal evolution of these impacts. Using extensive monitoring data from a crude oil spill site near Bemidji, Minnesota (USA), we implemented a comprehensive model that simulates secondary plumes of depleted dissolved O_2 and elevated concentrations of Mn^{2+}, Fe^{2+}, CH_4, and Ca^{2+} over a two-dimensional cross section for 30 years following the spill. The model produces observed changes by representing multiple oil constituents and coupled carbonate and hydroxide chemistry. The model includes reactions with carbonates and Fe and Mn mineral phases, outgassing of CH_4 and CO_2 gas phases, and sorption of Fe, Mn, and H^+. Model results demonstrate that most of the carbon loss from the oil (70%) occurs through direct outgassing from the oil source zone, greatly limiting the amount of CH_4 cycled down-gradient. The vast majority of reduced Fe is strongly attenuated on sediments, with most (91%) in the sorbed form in the model. Ferrous carbonates constitute a small fraction of the reduced Fe in simulations, but may be important for furthering the reduction of ferric oxides. The combined effect of concomitant redox reactions, sorption, and dissolved CO_2 inputs from source-zone degradation successfully reproduced observed pH. The model demonstrates that secondary water quality impacts may depend strongly on organic carbon properties, and impacts may decrease due to sorption and direct outgassing from the source zone.

1. Introduction and Motivation

Secondary water quality impacts (SWQIs) in contaminated aquifers consist of groundwater plumes that result from the degradation of a primary contaminant or organic amendment. Although secondary impacts are typically less harmful than the contaminant of concern, they can impair water quality, even after the original contaminant sources are attenuated. There is growing concern surrounding SWQIs at electron donor addition remediation sites, where organic substances are introduced into aquifers to stimulate biodegradation of chlorinated solvents [*AFCEE (Air Force Center for Environmental Excellence)*, 2004; *Borden*, 2007; *Cox*, 2009; *Stroo and Ward*, 2010], explosives and propellants (TNT, RDX, HMX, ClO_4^-) [*Rodgers and Bunce*, 2001; *Hatzinger*, 2005], selected metals and radionuclides (Cr[VI], TcO_4^-, UO_2^{2+}) [*Lloyd and Lovley*, 2001], and other contaminants. Secondary impacts of the intentionally injected organic substances must be considered for the development of responsible, effective, and sustainable remediation practices.

Secondary impact characterization is complicated by the need to consider a diverse range of coupled, indirect, and future outcomes following the introduction of the electron donor. Numerical reactive transport models that can represent multiple components and include a comprehensive set of secondary reactions triggered by organic degradation are essential for evaluating the overall consequences in contaminated subsurface systems (for reviews of such models, see *Hunter et al.* [1998], *Islam et al.* [2001], *Barry et al.* [2002], *Brun and Engesgaard* [2002], *Steefel et al.* [2005], and *Thullner et al.* [2007]). Biogeochemical models have provided important insights into contaminated groundwater sites. They have helped in identifying redox zonation and dominant terminal electron acceptors [*Prommer et al.*, 1999a; *Mayer et al.*, 2001; *Brun*

et al., 2002; *Vencelides et al.*, 2007]. Also, they have illustrated the major roles of nonaqueous phase processes, such as mineral dissolution and precipitation [*McNab and Narasimhan*, 1995; *van Breukelen et al.*, 2004; *Vencelides et al.*, 2007], sorption [*van Breukelen et al.*, 2004], outgassing [*Mayer et al.*, 2001; *van Breukelen et al.*, 2004; *Vencelides et al.*, 2007], gas bubble formation and entrapment [*Amos and Mayer*, 2006], and dynamic permeability feedbacks [*Singhal and Islam*, 2008; *Li et al.*, 2010]. Biogeochemical models have become common predictive and research tools at contaminant sites over the last couple of decades, but their site-specific implementation can remain a challenge due to limited field-scale observations, parameter values, and process understanding [*Steefel et al.*, 2005; *Thullner et al.*, 2007]. This is particularly the case at electron donor addition remediation sites, which are generally monitored for secondary water quality impacts, but are typically lacking in spatially extensive and long-term information.

SWQIs also result from biodegradation of hydrocarbons. Study sites for hydrocarbon natural attenuation provide strong launching points for developing a geochemical model suitable for probing secondary water quality impacts at electron donor addition remediation sites. Intensive monitoring and investigation have been carried out at the National Crude Oil Spill Fate and Natural Attenuation Research Site near Bemidji, Minnesota (USA) following a crude oil pipeline spill on 20 August 1979. The Bemidji site has been the subject of multidisciplinary studies by the U.S. Geological Survey Toxic Substances Hydrology program, many of which are described in the review by *Essaid et al.* [2011]. A number of geochemical modeling studies have been conducted to assess processes behind the hydrocarbon attenuation [*Bennett et al.*, 1993; *Baedecker et al.*, 1993; *Essaid et al.*, 1995; *McNab and Narasimhan*, 1995; *Curtis et al.*, 1999; *Curtis*, 2003; *Essaid et al.*, 2003; *Amos*, 2006; *Amos and Mayer*, 2006], making the Bemidji site an ideal test case with which to develop a model to investigate SWQIs.

Most of the previous Bemidji models have focused on the fate of hydrocarbons, especially BTEX (benzene, toluene, ethylbenzene, m,p-xylene, and o-xylene), and the emphasis has generally not been to fully represent degradation products and by-products or follow their fate. Many of these modeling studies lack data constraints on some of the secondary components of the model, such as mineral or gas phase observations. As a result, previous Bemidji models have each lacked certain processes and/or included simplified representations, which hampered their ability to represent the geochemical evolution of the plume, including many aquifer impacts that are secondary to the primary BTEX attenuation. In this study, we build off the previous Bemidji models listed above and develop a reactive transport model that is guided by diverse data types and updated measurements at the site. The new and/or improved components to the Bemidji model incorporate recent inferences by *Ng et al.* [2014], including detailed treatment of the oil source, new outgassing mechanisms, multiple pH buffering sources, and representation of sorption. The resulting comprehensive model is used to quantitatively evaluate the different biogeochemical processes that control the spatiotemporal evolution of both the primary organic carbon and secondary water quality groundwater plumes of depleted O_2 and elevated dissolved organic carbon, reduced metals, CH_4, and other major ions at the Bemidji site.

2. Bemidji Oil Spill Site

Over 30 years of data collected at the Bemidji site have demonstrated that persisting oil pools along the water table are ongoing sources of dissolved organic carbon and degradation products in the groundwater. Shortly after the spill, oxygen became depleted near the source, and anaerobic terminal electron accepting processes (TEAPs) involving Mn oxide minerals, Fe oxyhydroxide minerals, and methanogenesis became important [*Baedecker et al.*, 1993; *Cozzarelli et al.*, 2001]. The attenuation of the organic carbon in the aquifer has resulted in observed secondary plumes of depleted dissolved oxygen (DO) and elevated levels of dissolved Mn^{2+}, Fe^{2+}, and CH_4.

2.1. Previous Modeling Studies

Previous modeling studies have all focused on the Bemidji north pool transect, as does this model. One-dimensional modeling studies examining the effects of the oil biodegradation on inorganic chemistry [*Bennett et al.*, 1993; *Baedecker et al.*, 1993; *McNab and Narasimhan*, 1995; *Curtis et al.*, 1999; *Curtis*, 2003] have provided a number of important insights. *Bennett et al.* [1993] showed that aqueous concentrations of major cations could be largely explained by the addition of CO_2 from biodegradation and the dissolution or precipitation of various minerals at equilibrium. *Baedecker et al.* [1993] established the importance of CO_2 and CH_4 outgassing, the coupling between organic carbon degradation and Fe reduction, and

reprecipitation of reduced Fe. *McNab and Narasimhan* [1995] demonstrated the difficulty of simultaneously matching Fe^{2+} and pH data and the sensitivity of model results to the assumed ferric oxide mineral phase. *Curtis et al.* [1999] showed that simulating observed pH required the onset of methanogensis before the cessation of Fe reduction. *Curtis* [2003] found that the Monod kinetic modeling of multiple TEAPs can allow thermodynamically unfavorable reactions to proceed, resulting in large errors in pH. He further established that partial equilibrium [*Jakobsen and Postma*, 1999] or fully kinetic reactions with free energy dependencies successfully avoid these unrealistic simulations.

Two-dimensional cross section modeling studies by *Essaid et al.* [1995], *Essaid et al.* [2003], *Amos* [2006], and *Amos and Mayer* [2006] provided additional insights. *Essaid et al.* [1995] simulated sequential aerobic, Mn(IV)-coupled, Fe(III)-coupled, and methanogenic biodegradation of dissolved organic carbon (DOC) using multiple Monod kinetics with microbial growth. Their results showed that microbial growth was unimportant 5–10 years after the spill and confirmed that most of the reduced Mn and Fe are retained on sediments. *Essaid et al.* [2003] focused on modeling dissolution from the oil and biodegradation of BTEX. Using inverse modeling, they demonstrated the importance of dissolution properties and oil saturation on BTEX loss from the oil and the relative unimportance of seasonal recharge variation. The most comprehensive previous modeling was by *Amos* [2006], who modified the unsaturated/saturated zone reactive transport model MIN3P [*Mayer et al.*, 2002] to include bubble formation, contraction, and entrapment [*Amos and Mayer*, 2006]. A major contribution by *Amos* [2006] is the representation of redox-related gases in the saturated zone plume, including O_2 dissolution and CH_4 and CO_2 outgassing.

Although each of these models provided important insights, no single model included all of the following: dissolution and biodegradation of all forms of organic carbon from the oil source, multidimensional domain spatial effects, explicit mineral representations, inorganic reactions, sinks for reduced iron, and outgassing based on all dissolved gases. All of these processes are required to fully characterize dynamical processes starting from the degrading organic carbon source to the various geochemical phases that participate in the production and attenuation of the diverse secondary water quality species as they are transported through the aquifer. Our comprehensive model will be used to evaluate the relative importance of these different processes for SWQIs at Bemidji.

2.2. Data

Data used in this modeling study were chosen to span different time periods, to encompass diverse geochemical phases and constituents, and to serve distinct functions in guiding the model development. The four time periods (the time of the oil spill in 1979, 1987 ± 2 years, 1993 ± 2 years, and 2008 ± 2 years) were selected on the basis of data availability and to provide a representative sampling throughout the 30 year history of the spill. Table 1 lists the data used and the associated references. Descriptions of data methods and previously published data sets are presented in *Ng et al.* [2014].

Recent 2008 data on aqueous and gaseous degradation products and extensive sediment-associated reduced Fe (Fe(II)) observations were not considered in previous Bemidji modeling work. This is also the first modeling study to incorporate direct observations of temporal changes in oil source composition, thus providing a full accounting of the organic carbon sources driving secondary plume production. Oil data include analyses of a 1984 pipeline sample taken to represent the initial composition of the spilled oil and 2008 samples from five wells. In addition to volatile hydrocarbon data from *Baedecker et al.* [2011], we also analyzed the initial content of high molecular weight alkanes in a sample representative of the spilled oil. For the analysis, 10 μL of oil was diluted with 5 mL hexane and 1 μL of the mixture was analyzed by GC/MS on an Agilent 6890A GC interfaced with an Agilent 5973 MS using a 30 m DB-5 column with a coating thickness of 0.25 μm. The GC inlet temperature was 250°C and the column was programmed from 50°C to 300°C at 5°/min and held 10 min. The MS was operated with an ionizing energy of 70 eV at 250°C in full scan mode. An external standard comprised of 21 *n*-alkanes and pristane and phytane was used to quantify the data based on response of ion 57. Deuterated-*n*-C24 was added to the samples and standard to monitor instrument response.

3. Model Formulation

This study incorporates processes from previous Bemidji models, including diverse hydrocarbon compounds [*Essaid et al.*, 1995, 2003; *Amos*, 2006], mineral controls on anaerobic biodegradation [*Baedecker et al.*, 1993; *Curtis et al.*, 1999; *Curtis*, 2003; *Amos*, 2006], mineral controls on inorganic geochemistry [*Bennett*

Table 1. Bemidji North Pool Data Sources (adapted from *Ng et al.* [2014, Table 1])

	Data Type	Data Source(s)
Initial/ Background	Oil composition	Eganhouse et al. [1993], Baedecker et al. [2011], Thorn and Aiken [1998], this study
	Oil saturation[a]	1990, 1992: Essaid et al. [2003], 1998: Ng et al. [2014]
	Aqueous species[b]	Ng et al. [2014]
	Sediment-associated Fe[c]	Tuccillo et al. [1999]
1987$\pm$2	Dissolved BTEX[d]	Eganhouse et al. [1993], Baedecker et al. [1993]
	NVDOC[e]	Eganhouse et al. [1993], Baedecker et al. [1993]
	Aqueous species	Bennett et al. [1993], Baedecker et al. [1993]
	Sediment-associated Fe	Not available
1993$\pm$2	Dissolved BTEX	Cozzarelli et al. [2001]
	NVDOC	Cozzarelli et al. [2001]
	Aqueous species	O_2, CH_4 , Fe^{2+}: Cozzarelli et al. [2001], Others: Ng et al. [2014]
	Sediment-associated Fe	Tuccillo et al. [1999]
2008$\pm$2	Dissolved BTEX	Ng et al. [2014]
	NVDOC	Amos et al. [2012]
	Aqueous species	CH_4: Amos et al. [2011], Others: Ng et al. [2014]
	Sediment-associated Fe	2006-2007: Amos et al. [2012], 2008: Ng et al. [2014]
	CO_2 surface efflux	Sihota et al. [2011], Sihota et al. [2014]
	Oil fates	Baedecker et al. [2011], Thorn and Aiken [1998], Bekins et al. [2005]

[a]Data collected in 1990, 1992, and 1999 used to represent initial oil pool conditions.
[b]Includes dissolved O_2, pH, alkalinity, CH_4, Fe^{2+}, Mn^{2+}, Ca^{2+}, and Mg^{2+}.
[c]Includes 0.5 M HCl extractions for Fe(II) and Fe(III) measurements.
[d]Includes benzene, toluene, ethylbenzene, and xylene.
[e]Includes non-volatile dissolved organic carbon.

et al., 1993; *Curtis et al.*, 1999; *Amos*, 2006], multicomponent outgassing [*Amos*, 2006], and secondary chemical reactions such as full carbonate and hydroxide chemistry and (re)oxidation of reduced TEAP products [*McNab and Narasimhan*, 1995; *Curtis et al.*, 1999; *Curtis*, 2003; *Amos*, 2006]. To ensure valid thermodynamic reaction progression, these processes are implemented using the partial equilibrium approach following *Curtis* [2003]. Microbial growth is neglected based on the finding by *Essaid et al.* [1995] that populations stabilize early following the spill.

Based on gaps identified by a mass balance analysis of the Bemidji data in Table 1, *Ng et al.* [2014] proposed an updated conceptual model that requires additional mechanisms for carbon outgassing, dissolved inorganic carbon (DIC) inputs, pH buffering, and Fe(II) immobilization. As depicted in Figure 1, we develop a numerical model that tests and further develops these ideas through the following processes not considered in previous work on the Bemidji site:

1. Direct outgassing of CH_4 and CO_2 produced from oil constituents that degrade within the pore space adjacent to the entrapped oil (outgassing mechanism),

2. Dissolution of CO_2 that is produced from oil constituents degrading within the pore space adjacent to the entrapped oil (DIC source and pH buffer), and

3. Sorption of reduced Fe involving exchange with H^+ (pH buffer and Fe(II) immobilization).

Simulations over 30 years of the 2-D cross-sectional study domain along the Bemidji north pool transect are carried out using the reactive multicomponent transport model PHT3D [*Prommer et al.*, 2003], which couples groundwater flow from MODFLOW2005 [*Harbaugh*, 2005], the transport component of the model MT3DMS [*Zheng and Wang*, 1999], and the geochemical capabilities of PHREEQC-2 [*Parkhurst and Appelo*, 1999].

3.1. Model Domain and Flow Model
The model simulation period covers the time of the spill in August 1979 until December 2008. The study domain comprises a 260 m horizontal (45 m up-gradient of reference well 421–215 m down-gradient) and 7 m vertical (417–424 m elevation) cross section along the north pool transect. The computational grid was extended 260 m farther down-gradient and down to 410 m elevation to avoid boundary effects on simulations. The domain was discretized into 4.3 m (horizontal) by 0.47 m (vertical) grid cells allowing efficient computation of multicomponent kinetic simulations. The homogeneous porosity is assigned to be 0.38, which is the mean value determined for the north pool area [*Dillard et al.*, 1997]. Longitudinal and transverse dispersivity were set to 1 and 0.04 m, respectively.
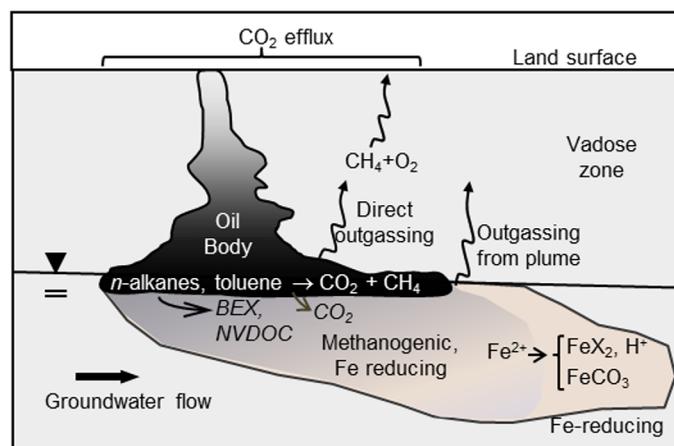
Figure 1. New conceptual model of the Bemidji north pool implemented with the reactive transport model. Included are processes not considered in previous Bemidji modeling studies, such as distinct degradation pathways for diverse oil constituents, direct outgassing in addition to outgassing from the aqueous phase, and Fe sorption with H^+ exchange. The model domain includes the oil body at and below the water table.

Heterogeneous permeability values based on geostatistical interpolation of grain size data are available from *Dillard et al.* [1997] down to an elevation of 421 m and over a 120 m horizontal interval of our domain. Permeability values were replicated to cover our computational domain and converted to saturated hydraulic conductivity. The conductivity was then inflated by a factor of two to yield a geometric mean of 5.1 m/d and arithmetic mean of 6.3 m/d for a closer match with the homogeneous 6.1 m/d determined in the inverse modeling of *Essaid et al.* [2003]. While the model is an approximate characterization of actual spatial variability, it incorporates realistic patterns and length scales of heterogeneity based on soil texture observations. We neglect multiphase flow and treat the oil phase as stationary in time, but, following *Essaid et al.* [2003], we represent the effect of partial oil saturation through the application of relative water permeability (k_{rw}):

$$k_{rw} = S_w^{0.5}(1-(1-S_w^{1/m})^m)^2, \tag{1}$$

where S_w is water saturation ($S_w = 1 - S_o$, where S_o is oil saturation), $m = (1 - (1/n))$, and n is a pore size distribution parameter set to 3.98. Also to account for the oil, we specify an effective porosity, defined as the volume of water per total grid cell volume, by scaling total porosity by the water saturation. A steady state flow field was produced with MODFLOW by imposing constant head boundary conditions consistent with an observed average water table gradient of 0.0035 m/m and left head boundary of 424 m elevation (above sea level), and a constant recharge rate of 4.88×10^{-4} m/d determined by the inverse modeling of *Essaid et al.* [2003]. The saturated conductivity field and resulting flow lines are shown in Figure 2a.

3.2. Geochemical Model Formulation
3.2.1. Model Components and Background Conditions
The aqueous components in the model include inorganic C (carbonate species), CH_4, DO, Mn, Fe, Ca, Cl, Na, H, and inert N. Mineral phase electron acceptors include pyrolusite (MnO_2) and amorphous ferric hydroxide ($Fe(OH)_3$), and rhodochrosite ($MnCO_3$) and siderite ($FeCO_3$) are allowed to precipitate. Calcite is also included for its involvement in the carbonate chemistry of the aquifer. The model represents sorption of Fe(II), Mn(II), and H^+. Dissolved gas phases for CO_2, CH_4, O_2, and inert N_2 are incorporated to simulate outgassing.

Our model representation of the oil body along the water table is based on interpolated oil saturation data at and below 424 m elevation [*Ng et al.*, 2014], as shown in Figure 2b. *Herkelrath* [1999] calculated about 40% of the total north pool oil volume to be located in the unsaturated zone, which is not included in our groundwater model. Gas concentration data show that unsaturated zone oil biodegrades anaerobically [*Chaplin et al.*, 2002; *Amos et al.*, 2005], but model sensitivity tests indicate insignificant recharge contributions to secondary groundwater plumes compared to biodegradation at and below the water table in the oil body. Organic carbon from the oil is represented in both dissolved and nonaqueous (immobile oil) forms following the definitions by *Ng et al.* [2014] based on oil observations by *Eganhouse et al.* [1993], *Thorn and Aiken* [1998], and *Baedecker et al.* [2011]. The degradable oil categories are (with representative stoichiometries in parentheses): BEX (C_6H_6) for combined benzene, ethylbenzene, and xylene; toluene (C_7H_8); pre-NVDOC ($C_{19}H_{24}O_6$) for oil phase precursors to NVDOC [*Thorn and Aiken*, 1998]; short-chain n-alkanes ($C_{11}H_{25}$); and long-chain n-alkanes ($C_{15}H_{32}$). The remaining unreactive oil pool is assigned a molar concentration calculated using an average molecular weight of 341 g/mol determined by *Baedecker et al.* [2011].
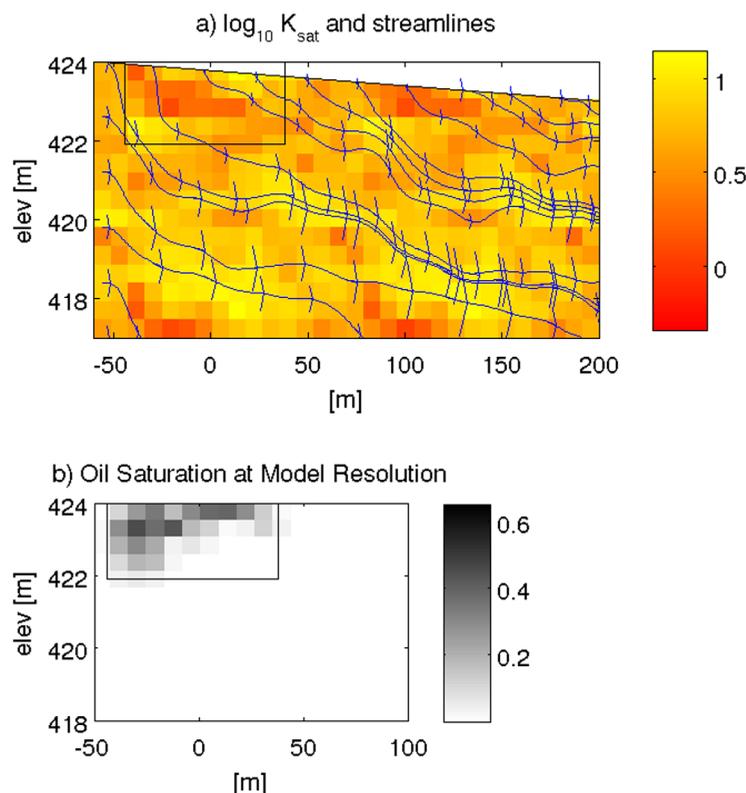
Figure 2. (a) Saturated hydraulic conductivity field ($\log_{10}$ (m/s)) and resulting steady state flow paths for the north pool transect study domain. In this and all following figures, horizontal distance is in reference to well 421, approximately at the center of the oil body, and elevation is shown using the NAVD29 standard. The reference rectangle indicates the area containing the oil body. (b) Oil saturation field interpolated from core data. Figure 2b is based on Figure 3 from *Ng et al.* [2014].

BEX are grouped together for simplicity due to their shared tendency to migrate in dissolved form before degrading. Using weighted-average stoichiometries, the short-chain *n*-alkane model compound represents all C_6-C_{12} *n*-alkanes, and the long-chain *n*-alkane model compound represents all C_{13}-C_{32} *n*-alkanes. Composition of the original oil [*Eganhouse et al.*, 1993] is combined with spatially distributed oil saturation measurements [*Essaid et al.*, 2003; *Ng et al.*, 2014] to produce the initial condition field for different degrading oil constituents (for details, see *Ng et al.* [2014]). We set the fraction of initial oil that is long-chain *n*-alkanes (f_{long}) to be 0.1. This number is based on new heavy molecular weight oil analyses indicating 5% of the initial oil is C_{13}-C_{32} *n*-alkanes. An additional 5% is included to account for *n*-alkane side chains attached to benzene, and cyclohexane, which also degrade under methanogenic conditions [*Hostettler and Kvenvolden*, 2002; *Hostettler et al.*, 2007]. The preNVDOC is derived from the remainder of the oil, which is estimated to be 40% of the original oil mass [*Eganhouse et al.*, 1993].

Initial condition aqueous concentrations were set according to background conditions from well 310e, located about 200 m up-gradient from the center of the oil body [*Ng et al.*, 2014]. Average background concentrations measured over six sampling times (over 1986–1995) were equilibrated with calcite and charge balanced using PHREEQC-2, which resulted in a downward adjustment of pH by about 0.1 due to calcite precipitation (see Table SI1 in supporting information). A sorption model, further discussed in section 4.2.6, was also initialized with the equilibrium background pH. For all aqueous species, a concentration flux boundary condition was implemented at the water table by specifying recharge with background concentrations. Dissolved O_2 concentrations in recharge were further reduced by half in oil body grid cells, as well as those up-gradient due to biodegradation in an up-gradient spray zone. The constant head boundary condition at the up-gradient left side was set to constant background concentrations.

Mineral Fe concentrations are based on a 0.5 M HCl extraction method described by *Tuccillo et al.* [1999]. Initial $Fe(OH)_3$ concentration of 0.0393 mol/L_v (L_v is bulk or total aquifer volume in liters) was determined from average background samples measurements of Fe(III) [*Tuccillo et al.*, 1999] and assuming a bulk density of 1650 g/L_v. We consider 0.0288 mol/L_v of that amount to be bioavailable for redox coupling, based on the average 0.0105 mol/L_v Fe(III) remaining near the oil body (average within 100 m) 30 years after the spill [*Amos et al.*, 2012; *Ng et al.*, 2014]. Using low Mn oxide extraction results of $\ll 1.5$ μmol/g (0.0025 mol/L_v assuming a bulk density of 1650 g/L_v) by M.E. Tuccillo (personal communication, 1997) as an upper-bound guideline, initial bioavailable pyrolusite (MnO_2) was set to 0.001 mol/L_v to produce the observed elevated aqueous Mn^{2+} concentrations of approximately 5×10^{-5} mol/L.

3.2.2. Partial Equilibrium Redox Model

The model uses the partial equilibrium approach of *Jakobsen and Postma* [1999], which assumes that the organic carbon oxidation step is the rate-limiting step, and the corresponding reduction step may be represented as equilibrium reactions. Following *Prommer et al.* [1999b], this is implemented in PHT3D by kinetically and irreversibly adding organic carbon compounds by their constitutive elements and known valence states. For example, for one mole of benzene (C_6H_6) degrading at a specified rate, six moles of C(-1) and six moles of H($+1$) are newly introduced into the equilibrium solution (oxidation states in parentheses). C(-1) then automatically converts to the inorganic carbon form via the TEAP with the most favorable equilibrium thermodynamic conditions in the solution. This model implementation is equivalent to organic carbon fully fermenting to H_2 and CO_2 at a determined rate, and then H_2 becoming consumed by multiple aqueous and mineral phase TEAPs controlled by their equilibrium constants. Specifically, the equilibrium redox couples needed to simulate the secondary plumes at Bemidji are H^+/H_2, O_2/H_2O, Fe(III)/Fe(II), Mn(IV)/Mn(II), and CO_2/CH_4. Other aqueous phase equilibrium reactions considered include those found in the PHT3D database, such as full carbonate and hydroxide chemistry and reoxidation.

3.2.3. Organic Carbon Degradation

In order to use oil body observations to constrain the model, we represent organic carbon dissolution kinetics starting from four oil constituents: BEX, toluene, long and short-chain *n*-alkanes, and oil constituents contributing to NVDOC (preNVDOC). We tailor the expression of the degradation process of each to follow the pathways described in *Ng et al.* [2014]. Other hydrocarbon modeling studies have separately represented the different compounds comprising the bulk mixture and showed that implementing unique degradation parameters for each strongly affects the overall simulations [*Nicol et al.*, 1994; *D'Affonseca et al.*, 2011]. Similar to *Essaid et al.* [2003] and *Curtis et al.* [1999], BEX is assumed to follow a multicomponent dissolution rate (Table 2):

$$r_{diss,BEX} = k_{diss,BEX} * (C_{sat,mc,BEX} - C_{BEX}), \tag{2}$$

where $r_{diss,BEX}$ (mol/L_w/s) (L_w is volume of pore water in liters) is the rate at which BEX dissolves into the aqueous phase, $k_{diss,BEX}$ (s^{-1}) is the first-order kinetic dissolution coefficient, $C_{sat,mc,BEX}$ (mol/L_w) is the multicomponent solubility of BEX, and C_{BEX} (mol/L_w) is the concentration of dissolved BEX. The multicomponent solubility follows Raoult's law:

$$C_{sat,mc,BEX} = C_{sat,BEX} * \frac{C_{BEXnapl}}{C_{totnapl}}, \tag{3}$$

where $C_{sat,BEX}$ (mol/L_w) is the single-species solubility of BEX, $C_{BEXnapl}$ (mol/L_w) is the concentration of nonaqueous phase BEX, and $C_{totnapl}$ (mol/L_w) is the total concentration of all nonaqueous phase components in the oil.

In the partial equilibrium implementation, kinetic rates are established only for the oxidation half reaction of organic carbon degradation, or equivalently, the completed fermentation reactions to H_2 and inorganic carbon shown in Table 2. Note that although inorganic carbon is the immediate product shown, CH_4 may be the end form when it is the thermodynamically favorable TEAP in the partial equilibrium approach. As further detailed below, *n*-alkane oxidation is treated differently, with kinetic rates set explicitly for methanogenic biodegradation (Table 2). We assume a first-order kinetic rate for each organic carbon component:

$$\frac{dC_{OC_i}}{dt} = -k_{OC_i} C_{OC_i}, \tag{4}$$

where k_{OC_i} is the first-order rate coefficient for the ith organic carbon component, and C_{OC_i} is the concentration of that organic carbon component. In this partial equilibrium approach, organic carbon degradation follows the same kinetic rate law for both aerobic and anaerobic TEAPs, which we consider reasonable given the dominance of anaerobic biodegradation over the 30 years following the spill. For BEX biodegradation, equation (4) is applied with a coefficient k_{BEX} and with C_{OC_i} as the aqueous phase concentration of BEX.

Ng et al. [2014] described oil-contact degradation (adjacent to the oil) for toluene and *n*-alkanes, which is simulated by allowing degradation to occur directly from their nonaqueous forms following equation (4), with first-order rates (k_{Tol}, $k_{nAlk,S}$, and $k_{nAlk,L}$) defined with respect to nonaqueous phase concentrations (Table 2). Aqueous phases of toluene and *n*-alkanes are not represented in the model, which is consistent

Table 2. Model Implementation of Oil Constituents

Kinetic Reactions	Kinetic parameters[a]
BEX (C_6H_6)	
$\quad BEX_{NAPL} \rightarrow BEX_{aq}$	$k_{diss,BEX}, C_{sat,BEX}$
$\quad BEX_{aq} + 18H_2O \rightarrow 6HCO_3^- + 15H_2 + 6H^+$	k_{BEX}
Toluene (C_7H_8)	
$\quad Tol_{NAPL} + 21H_2O \rightarrow 7HCO_3^- + 18H_2 + 7H^+$	k_{Tol}
NVDOC ($C_{19}H_{24}O_6$)	
$\quad preNVDOC_{NAPL} \rightarrow NVDOC_{aq}$	$k_{preNVDOC}, k_{inhib}$
$\quad NVDOC_{aq} + 51H_2O \rightarrow 19HCO_3^- + 44H_2 + 19H^+$	k_{NVDOC}
Short chain n-alkanes ($C_{11}H_{25}$)	
$\quad nAlkS_{NAPL} + 4.75H_2O \rightarrow 8.625CH_4 + 2.375CO_2$	$k_{nAlk,S}$
Long chain n-alkanes ($C_{15}H_{32}$)	
$\quad nAlkL_{NAPL} + 7H_2O \rightarrow 11.5CH_4 + 3.5CO_2$	$k_{nAlk,L}$

[a]Manually calibrated values for the kinetic parameter are provided in Table 3.

with the absence of these dissolved compounds in the plume [*Eganhouse et al.*, 1993], large surface carbon dioxide efflux, and dissolved gas data.

With little theoretical guidance for representing the breakdown of the complex preNVDOC pool, we include a two-part implementation of the first-order degradation model. The first part represents the kinetic partial degradation of immobile preNVDOC to aqueous phase NVDOC ($k_{preNVDOC}$), and the second part implements a distinct coefficient for subsequent degradation of NVDOC to carbonate species and H_2 (k_{NVDOC}) (Table 2). In order to produce the observed increase in NVDOC by the end of the 30 years (see Figure 1 in the supporting information), we pose a conceptual model in which formation of NVDOC from preNVDOC in the oil is inhibited by competition with toluene and n-alkanes, which also degrade under methanogenic conditions adjacent to the oil body. *Thorn and Aiken* [1998] found large alkylaromatic oil constituents to be likely precursors to NVDOC, and these aromatic molecular structures may support shared enzyme use and competition. Furthermore, proposed anaerobic pathways for n-alkane degradation [*Callaghan*, 2013] and inferred partial degradation intermediates for toluene [*Cozzarelli et al.*, 1990] both involve hydroxylation of methyl groups, lending additional credibility for related enzymatic activity. The partial degradation rate of preNVDOC to NVDOC ($r_{preNVDOC}$) (Table 2) depends on the nonaqueous phase concentration of preNVDOC ($C_{preNVDOC}$):

$$r_{preNVDOC} = \frac{k_{preNVDOC}}{I_{nAlk,S}I_{nAlk,L}I_{Tol}}C_{preNVDOC}, \tag{5}$$

with noncompetitive inhibition terms due to short-chain n-alkanes, long-chain n-alkanes, and toluene, respectively:

$$I_{nAlk,S} = 1 + \frac{C_{nAlk,S}}{k_{inhib}}$$

$$I_{nAlk,L} = 1 + \frac{C_{nAlk,L}}{k_{inhib}} \tag{6}$$

$$I_{Tol} = 1 + \frac{C_{Tol}}{k_{inhib}},$$

where k_{inhib} is a noncompetitive inhibition constant, and $C_{nalk,S}$, $C_{nalk,L}$, and C_{Tol} are, respectively, the concentrations of nonaqueous phase short-chain n-alkanes, long-chain n-alkanes, and toluene. We assign identical inhibition constants to the three constituents, given the assumed similar enzymatic activity described above.

Dissolution and degradation rate coefficients for quantified oil components are determined using observed fractional depletions of different oil components [*Baedecker et al.*, 2011; *Bekins et al.*, 2005]. Final parameter estimates are provided in Table 3. The observed 60% of benzene lost from the oil through dissolution by 2008 [*Baedecker et al.*, 2011] translates to 13% BEX lost, assuming insignificant loss of ethylbenzene and xylene. The first-order kinetic dissolution rate coefficient for equation (2) and degradation rate coefficient

for equation (4) are calibrated to this and dissolved BEX data, as well as other plume features. For simplicity, the single-component, pure-phase solubility of benzene (0.02282 mol/L) was adopted for BEX, given that benzene is by far the most soluble of the three species and 70–80% of the other constituents remained in the oil in 2008 [*Baedecker et al.*, 2011]. Toluene had nearly entirely been depleted from the oil by 2005 [*Baedecker et al.*, 2011], but matching this rate yields too much decay in 1988, when the average value observed at 5 wells was 3.2 mg/g. Instead, we set the degradation rate coefficient to 3.5×10^{-9} s^{-1}, which yields 2.1 mg/g in 1988 and 4% remaining in 2008. We set a first-order decay rate coefficient of 7.6×10^{-10} s^{-1} for short-chain *n*-alkanes, based on observations that they are on average about 50% depleted by 2008 [*Baedecker et al.*, 2011]. The degradation rate of long-chain *n*-alkanes is more uncertain. We visually approximated 50% degraded over 20 years from gas chromatograph results in *Bekins et al.* [2005] and determined a corresponding first-order rate coefficient of 1.1×10^{-9} s^{-1}. Due to a lack of data on the loss of oil precursors to NVDOC, parameters for preNVDOC and NVDOC are adjusted to match aqueous observations.

For comparisons with literature values, kinetic parameters used for BEX in this study should approach those for benzene alone, given the very low solubility and observed loss of ethylbenzene and xylene from the oil. Our field-calibrated first-order degradation coefficient for BEX ($k_{BEX} = 1.00 \times 10^{-8}$ s^{-1}) is comparable in magnitude to anaerobic rates previously found for Bemidji using well data (4.28×10^{-8} s^{-1}) [*Cozzarelli et al.*, 2010] and inverse modeling for the site (2.00×10^{-8} s^{-1} for the iron-reducing case) [*Essaid et al.*, 2003]. Compared to estimates for other sites, our value is within the lower end of microcosm and field estimates compiled by *Suarez and Rifai* [1999] (0 to 3.94×10^{-7} s^{-1}, mean 1.04×10^{-7} s^{-1}) and is closer to mean values found from the inverse model of *Lønborg et al.* [2006] (1.85×10^{-8} s^{-1}) and field values collected by *Aronson and Howard* [1997] (1.22×10^{-8} s^{-1}).

Direct measurements of dissolution coefficients are generally not available for the high flow rates found at Bemidji. Our adjusted value for first-order BEX dissolution ($k_{diss,BEX} = 6.31 \times 10^{-9}$ s^{-1}) is lower than the inverse modeling value of *Essaid et al.* [2003] (7.6×10^{-8} s^{-1}); however, in their simulations, total nonaqueous components did not change with time, which leads to underestimated multicomponent solubility at later times. *Essaid et al.* [2003] also noted that their initial effective (multicomponent) solubility was likely too low, because it was based on maximum aqueous-phase equilibrium data and not constrained by oil composition observations. The above studies with benzene degradation rates also provided results for toluene, but evaluation against these literature values is not straightforward because our first-order degradation model for toluene is defined relative to oil phase concentrations rather than the standard aqueous form. In addition, there is high uncertainty in degradation estimates for dissolved toluene because of very low observed concentrations [*Cozzarelli et al.*, 2010].

Methanogenic degradation of *n*-alkanes has been demonstrated [*Anderson and Lovley*, 1999; *Zengler et al.*, 1999], but there have been few efforts to estimate rates. First-order rate coefficients determined for *n*-alkanes by *Siddique et al.* [2008] were about 10–50 times greater than our calibrated parameters. There is no basis for evaluating parameters for our novel NVDOC model with inhibited dissolution of preNVDOC.

3.2.4. Direct Outgassing Adjacent to the Oil Body

Characterizing aqueous phase impacts requires proper representation of the significant carbon loss through outgassing. Our proposed conceptual model includes direct outgassing of CO_2 and CH_4 from the oil body source zone in order to match surface efflux measurements from *Sihota* [2014]. In the model, we attribute this mechanism to poorly soluble short and long-chain *n*-alkanes that degrade in pore spaces within the oil body. Similar to *n*-alkanes, we approximate toluene degradation as occurring adjacent to the oil body without an intermediary aqueous phase in the model. However, because toluene is observed to be more soluble than *n*-alkanes, we allow its degradation products to enter into the aqueous equilibrium solution rather than directly outgas.

The directly outgassed products at the water table include both CO_2 and CH_4, but CH_4 is oxidized to CO_2 before reaching the land surface [*Amos et al.*, 2005]. Using C efflux measured at the land surface over the period of June 2011 to July 2013, *Sihota* [2014] determined a seasonally weighted annual average due to oil degradation of 1.3 μmol/m^2/s. The observed surface efflux includes contributions from the vadose zone, which was not represented in our groundwater model. We attribute 60% of the surface efflux to the modeled oil body at and below the water table, based on spatial calculations by *Herkelrath* [1999] of the amount of oil near the water table versus in the vadose zone. Applying this fraction results in 0.78 μmol/m^2/s efflux,

Table 3. Organic Carbon Parameters

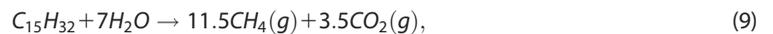|	Value	Equation	Reference
Bulk Oil			
Density (g/cm^3)	0.854	n/a	*Essaid et al.* [1993]
Initial total mass (g/m)	7.77×10^6	n/a	Derived with oil saturation data from *Essaid et al.* [2003] and *Herkelrath* [1999]
BEX (C$_6$H$_6$)			
Mass fraction of initial oil	0.010	n/a	Derived with BEX data from *Baedecker et al.* [2011]
$C_{sat,BEX}$ (single-component solubility) (M)	0.02282	(3)	Pure phase benzene
$k_{diss,BEX}$ (first-order dissolution coefficient) (1/s)	6.31×10^{-9}	(2)	Calibrated
k_{BEX} (first-order degradation coefficient) (1/s)	1.00×10^{-8}	(4)	Calibrated
Toluene (C$_7$H$_8$)			
Mass fraction of initial oil	0.0035	n/a	*Baedecker et al.* [2011]
k_{Tol} (first-order degradation coefficient) (1/s)	3.50×10^{-9}	(4)	Derived with oil loss data from *Baedecker et al.* [2011]
preNVDOC and NVDOC (C$_{19}$H$_{24}$O$_6$)			
Mass fraction of initial oil	0.40	n/a	Derived with oil data from *Eganhouse et al.* [1993]
$k_{preNVDOC}$ (first-order degradation coefficient) (1/s)	$1.18 \times 10{-}5$	(5)	Calibrated
k_{inhib} (inhibition constant) (M)	1.63×10^{-4}	(6)	Calibrated
k_{NVDOC} (first-order degradation coefficient) (1/s)	1.47×10^{-8}	(4)	Calibrated
Short-Chain n-Alkanes (C$_{11}$H$_{25}$)			
Mass fraction of initial oil	0.074	n/a	Derived with n-alkane data from *Baedecker et al.* [2011]
$k_{nAlk,S}$ (first-order degradation coefficient) (1/s)	7.60×10^{-10}	(4)	Derived with oil loss data from *Baedecker et al.* [2011]
g (dissolved CO$_2$ per mole degraded) (mol)	1.5	(10)	Calibrated
Long-Chain n-Alkanes (C$_{15}$H$_{32}$)			
f_{Long} (Mass fraction of initial oil)	0.1	n/a	This study's data
$k_{nAlk,L}$ (first-order degradation coefficient) (1/s)	1.10×10^{-9}	(4)	Based on chromatograph data from *Bekins et al.* [2005]
h (dissolved CO$_2$ per mole degraded) (mol)]	0.1	(11)	Calibrated

which we use to constrain the direct outgassing rates in the model. For short-chain *n*-alkane degradation, the fermentation reaction can be written as:
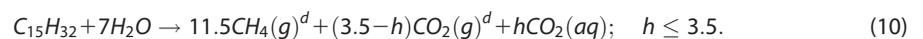
$$C_{11}H_{25} + 4.75H_2O \rightarrow 8.625CH_4(g) + 2.375CO_2(g), \tag{7}$$

where CH$_4$ and CO$_2$ are considered to be gases based on the high CO$_2$ efflux observed. However, for CO$_2$(g), the DIC data suggest that some of the CO$_2$ dissolves into the groundwater. Assuming that g moles of aqueous CO$_2$ are produced per mole of C$_{11}$H$_{25}$, and the rest remains a gas, the reaction becomes:

$$C_{11}H_{25} + 4.75H_2O \rightarrow 8.625CH_4(g)^d + (2.375 - g)CO_2(g)^d + gCO_2(aq); \quad g \leq 2.375. \tag{8}$$

All of the gaseous CH$_4$ and CO$_2$ produced by this reaction are outgassed directly (indicated with the superscript *d*), and the aqueous CO$_2$ helps to buffer the groundwater pH. The fermentation of long-chain *n*-alkanes can be written using a similar approach:

$$C_{15}H_{32} + 7H_2O \rightarrow 11.5CH_4(g) + 3.5CO_2(g), \tag{9}$$

and with outgassing and dissolved CO$_2$:

$$C_{15}H_{32} + 7H_2O \rightarrow 11.5CH_4(g)^d + (3.5 - h)CO_2(g)^d + hCO_2(aq); \quad h \leq 3.5. \tag{10}$$

Dissolution of a fraction of produced CO$_2$ is consistent with its high aqueous solubility, and it helps to achieve observed DIC concentrations and low pH in simulations without incurring higher than measured dissolved CH$_4$ concentrations. Greater occurrence of aqueous CO$_2$ compared to CH$_4$ is in line with findings in previous Bemidji studies. *Amos et al.* [2005] required 4 times more CO$_2$ input than CH$_4$ to match observed partial pressure values in their degassing batch model. *Revesz et al.* [1995] calculated from isotopic fractionation measurements an unexplained 2.4 times more CO$_2$ produced than CH$_4$ consumed by oxidation. Excess ratios of CO$_2$ to CH$_4$ can occur if methanogenic degradation is partially stalled at intermediary stages, although site data supporting this mechanism are not available.

Data are insufficient to uniquely calibrate the respective contributions from the two separate *n*-alkane model constituents to dissolving CO$_2$. We find that a total dissolution of 0.054 moles CO$_2$ per mole C from both *n*-alkane sources provides reasonable matches to efflux and plume observations. We attribute more CO$_2$ dissolution to the better-constrained short *n*-alkane degradation, setting $g = 1.5$ and $h = 0.1$, though the distribution between g and h does not significantly affect other processes in the model.

3.2.5. Outgassing From Solution

In the model, all CO_2 and CH_4 produced from the biodegradation of BEX, toluene, and NVDOC enter the aqueous solution, unlike from n-alkane biodegradation in the oil body, which generates direct outgassing. However, aqueous plumes of CO_2 and CH_4 are strongly controlled by their outgassing, which has been found to occur based on dissolved gas measurements [*Revesz et al.*, 1995; *Amos et al.*, 2005]. Following the degassing batch model implemented in *Amos et al.* [2005], we allow outgassing to occur in the model once the sum of the partial pressures of CO_2, CH_4, and N_2 reaches 0.93 atm, the average atmospheric pressure at 425 m elevation. Each gas species outgasses at a molar rate that is proportional to its partial pressure fraction of the total pressure. The same pressure threshold was applied to the entire domain, which we considered reasonable given that most outgassing occurs around the oil body near the water table [*Amos et al.*, 2005]. Complex and detailed treatment of bubble formation and collapse [*Amos and Mayer*, 2006] and gas phase transport through the vadose zone [*Amos*, 2006] were beyond the scope of this work. Without a vadose zone component in the model, we assume all gas phase CO_2 and CH_4 simulated in the aquifer and the oil body flux out of the land surface.

3.2.6. Solid Phase Processes

Solid phase processes and parameters implemented are summarized in Table 4. $Fe(OH)_3$ and pyrolusite are treated as equilibrium phase minerals. $Fe(OH)_3$ represents freshly precipitated ferric oxyhydroxide that is arguably much more unstable than the background Fe minerals in the aquifer. The $Fe(OH)_3(a)$ dissolution reaction log K in the PHT3D database (4.891) was lowered (0.239) just enough to produce the observed early appearance of CH_4 and low pH in simulations while allowing $Fe(OH)_3(a)$ dissolution. Pyrolusite is both a smaller reservoir of electron acceptors and is reduced with less pH impact (per electron accepted), and the original database log K value for the half reaction of pyrolusite reduction provided reasonable matches to the data.

Model representations of carbonate minerals are based on saturation indices determined using PHREEQC-2 batch simulation results shown in Figure 3. Based on consistent saturation indices near 0 throughout the domain for calcite, the system is modeled to be in equilibrium with calcite. *Bennett et al.* [1993] also identified dolomite as important for controlling background aquifer conditions, but considering its uncertain but likely slow dissolution properties [*Morse and Arvidson*, 2002], we treat it as nonreactive over the decadal time scale of this study.

Extraction studies [*Tuccillo et al.*, 1999] and modeling studies [*Baedecker et al.*, 1993; *Essaid et al.*, 1995] showed that nearly all reduced Fe mobilized by dissimilitory Fe reduction was rapidly immobilized on sediments. To represent the possible sinks of reduced forms through precipitation, we include the mineral phases of siderite ($FeCO_3$) and rhodochrosite ($MnCO_3$). We simplify the model implementation by omitting magnetite, which is limited to locations within the oil body [*Atekwana et al.*, 2014]. Siderite has been detected in the reduced zones of the Bemidji plume [*Baedecker et al.*, 1992; *Tuccillo et al.*, 1999; *Zachara et al.*, 2004], but saturation indices of siderite and rhodochrosite, using the PHREEQC-2 database dissolution log K values of -10.89 and -11.13 for siderite and rhodochrosite, respectively, are often above zero within the plume (Figure 3). This may suggest a kinetically limited precipitation model [*Jensen et al.*, 2002], but we choose instead to apply in-plume saturation indices determined with the original database (Figure 3) to adjust the dissolution log K values upward (Table 4). Because Mn reoxidation is significantly slower than Fe reoxidation [*Martin*, 2005], we do not allow it in the model implementation.

Previous Bemidji modeling studies that have included removal of reduced Fe and Mn from solution have attributed this effect to mineral precipitates [*Bennett et al.*, 1993; *Essaid et al.*, 1995]. Mass balance calculations indicate that a large and potentially unlikely amount of DIC would be removed if all sediment-associated Fe(II) occurred as siderite [*Ng et al.*, 2014], supporting the importance of alternative immobilization processes. Ferric oxide minerals and organic substances have significant Fe sorption capacity. *Tuccillo et al.* [1999] detected possible organically sorbed Fe(II) using Na-pyrophosphate extractions on Bemidji sediments, and *Zachara et al.* [2004] noted significant amounts of ion exchangeable Fe(II). Sorption of Fe(II) on sediment surface sites is a well-recognized phenomenon [*Liger et al.*, 1999], but quantitative characterization in natural environments can be difficult due to high sensitivity to oxygen exposure and interaction with other cations [*Hiemstra and van Riemsdijk*, 2007]. The importance of sorbed Fe(II) at Bemidji has not been explored or quantified. Some modeling studies of other anaerobic biodegradation sites explicitly consider Fe sorption [e.g., *Prommer et al.*, 1999a; *Brun et al.*, 2002; *van Breukelen et al.*, 2004; *Miles et al.*, 2008],

Table 4. Solid Phase Parameters

		$\log_{10}K$	Reference
Equilibrium Mineral Phases			
$Fe(OH)_3$	$Fe(OH)_3 + 3H^+ \leftrightarrow Fe^{3+} + 3H_2O$	0.239	Calibrated
Pyrolusite	$MnO_2 + 4H^+ + 2e^- \leftrightarrow Mn^{2+} + 2H_2O$	41.38	PHT3D database
Siderite	$FeCO_3 \leftrightarrow Fe^{2+} + CO_3^{2-}$	−9.35	Adjusted[a]
Rhodochrosite	$MnCO_3 \leftrightarrow Mn^{2+} + CO_3^{2-}$	−10.13	Adjusted[a]
Calcite	$CaCO_3 \leftrightarrow Ca^{2+} + CO_3^{2-}$	−8.48	PHT3D database
Sorption by Cation Exchange Model[b]			
Fe(II)	$Fe^{2+} + 2X^- \leftrightarrow FeX_2$	−4.03	Calibrated
Mn(II)	$Mn^{2+} + 2X^- \leftrightarrow MnX_2$	−4.03	Calibrated
H^+	$H^+ + X^- \leftrightarrow HX$	0	Set

[a]Model implementation of siderite and rhodochrosite dissolution $\log_{10}K$ values are PHREEQC-2 database values adjusted upward to approximate saturation index values calculated within the plume using the original database values (see Figure (3)).
[b]Sorption site X: calibrated cation exchange capacity of 0.0475 mol/Lv (Lv is volumetric liters of total aquifer).
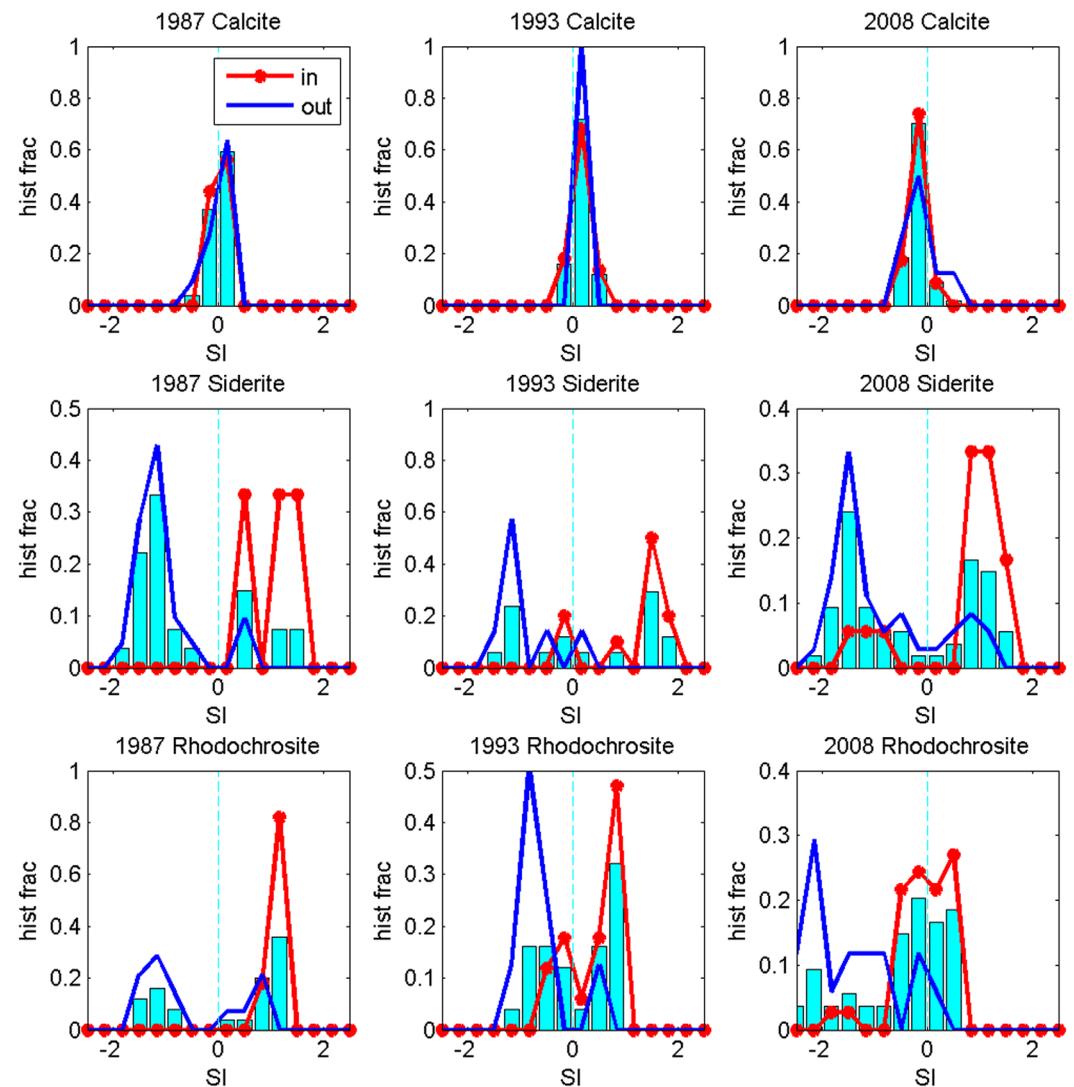

Figure 3. Histograms (normalized counts) for saturation index (SI) values calculated using PHREEQC-2 and original database dissolution logK values. Bars are for all well observations in the domain, "in" is for observations within the plume, and "out" is for observations outside the plume. The "plume" is defined as the area with elevated levels of the major cation for the corresponding mineral phase.

but many do not [e.g., *Mayer et al.*, 2001; *Vencelides et al.*, 2007; *D'Affonseca et al.*, 2011], including previous Bemidji modeling studies. *Essaid et al.* [1995] included uptake coefficients in their model that allowed for the majority of reduced Fe to remain on the sediments, but the form of the solid phase fraction was not modeled. We include surface reactions in our simulations to evaluate the conceptual model posed by *Ng et al.* [2014], in which sorption immobilizes Fe(II) and exchanges with H^+.

A diverse set of surface processes, including multiple site properties and complex electron transfer, likely occur. However, with little data to constrain a detailed surface model, we implement an effective parameterization of surface interactions that can produce the observed plume evolution. Surface site reaction models include ion exchange, mostly on clays [*Fletcher and Sposito*, 1989], and surface complexation, mostly on metal oxide phases, aluminosilicates, quartz, and edges on clay minerals [*Davis and Kent*, 1990]. The abundant metal oxide minerals at Bemidji support the occurrence of surface complexation. A complication to modeling adsorbed Fe(II) is that it can transfer an electron to an Fe(III) mineral structure [*Jeon et al.*, 2003], which could lead to a change in surface properties such as cation adsorption affinity [*Pedersen et al.*, 2005]. For our empirical sorption model, we elect to approximate cation sorption using a simple ion exchange model, which requires one less parameter than a surface complexation model. Prompted by observations of abundant sediment-bound Fe(II) and low pH, we include Fe^{2+}, Mn^{2+}, and H^+ in the surface reactions. A cation exchange capacity of 0.0475 mol/L_v was chosen to allow for the possibility of the majority of immobilized Fe(II) to appear as FeX_2. Assuming similar sorption behavior of Mn(II), we implement the same manually calibrated sorption logK parameter (-4.03) for both metals (Table 4).

Clays that exchange cations typically also involve Ca^{2+} and Mg^{2+} [*Fletcher and Sposito*, 1989; *Charlet and Tournassat*, 2005]. However, overlapping orbitals between Fe/Mn and the surface are stronger bonds than electrostatic attractions with Ca/Mg; also, the one to 2 orders of magnitude greater concentrations of Ca^{2+} and Mg^{2+}, compared to Fe^{2+}, complicate the adjustment of the sorption model for the Bemidji site. We thus omit Ca^{2+} and Mg^{2+} in our simplistic sorption model to facilitate matching observed concentrations of Fe and Mn. Fe and Mn plume evolutions are SQWI's of major concern, because these are redox species directly impacted by anaerobic biodegradation, and they have secondary water quality standards recommended by the EPA.

4. Model Simulation Results and Discussion

Cross-sectional simulation results are presented at three times that correspond closely to the postspill observation time periods: 2500 days (1986), 5000 days (1993), and 10,000 days (2007). To compare simulations against observations, normalized residuals are used:

$$residual_i = \frac{y_i - x_i}{R}, \tag{11}$$

where x_i is the model result at location index i, y_i is the collocated observation, and the normalization factor R is the maximum observed deviation from background conditions over the three observational periods. According to this equation, a positive residual indicates that the observation is higher than the simulated value.

4.1. Aqueous Phase Simulations

Figure 4 shows the full plume simulations of major aqueous redox species, including aqueous form electron donors (BEX, NVDOC), anaerobic electron acceptors (Mn^{2+}, Fe^{2+}, and CH_4), and DIC, which is produced with all TEAPs in the model. The simulations successfully capture the observed shift in importance from dissolved volatile organic carbon (BEX) to NVDOC. The model also simulates the observed slow growth of the Mn^{2+} and Fe^{2+} plumes and recent concentration decreases near the source. The early appearance of CH_4 and limited growth of the CH_4 plume are reproduced. Finally, the rapid growth and high concentrations of the DIC plume are matched.

Figure 5 shows residuals corresponding to Figure 4, and Figure 6 shows residuals for other important groundwater parameters (DO and pH) and cation contributor (Ca^{2+}). SWQI motivations focus less on Ca^{2+} compared to the redox species of Fe and Mn, as described above in section 3.2.6, but examining simulated Ca^{2+} results provides some assessment of how suitable our simple solid phase model is for representing overall aqueous geochemistry data. To further facilitate comparison of simulation results with data, figures
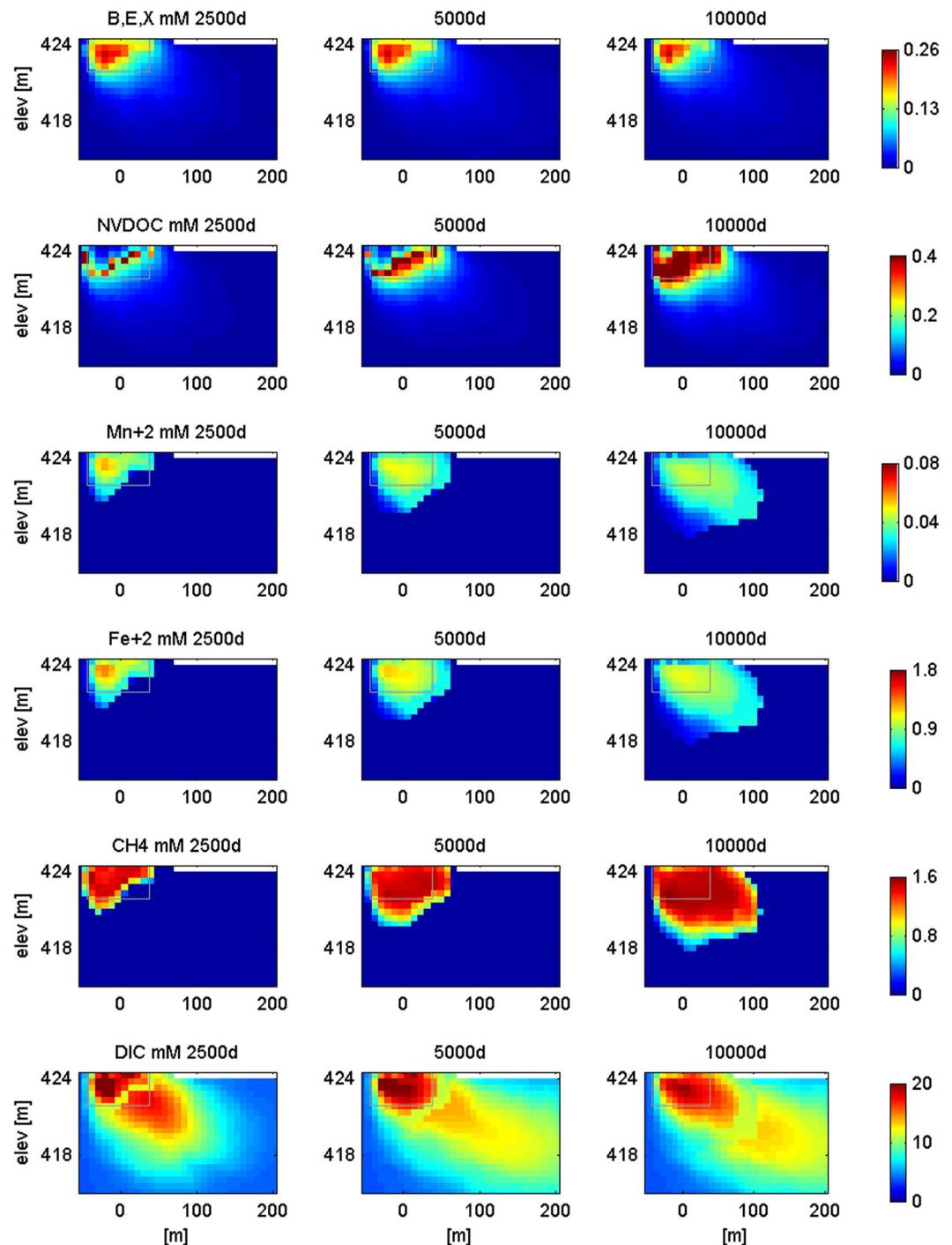
Figure 4. Model simulation results for six major redox species at three times corresponding to the observational time periods chosen for the data compilation. Gray boxes correspond to the oil body reference rectangle. BEX and NVDOC represent electron donors. Mn^{2+}, Fe^{2+}, and CH_4 are reduced aqueous species resulting from different anaerobic TEAPs. DIC is produced by all TEAPs.

showing residuals at available observation locations also have superimposed on them outlines of the observed plume. The plume outline is drawn as a convex polygon around wells or cores with measurements that are significantly different than background levels (further details on the plume delineation are provided in *Ng et al.* [2014]). The supporting information includes figures showing simulations and observations at the well locations (Figure SI1–SI4), which are used for calculating the residuals for Figures 5 and 6. Full simulated plume figures of DO and Ca^{2+} are also in the supporting information (Figure SI5)
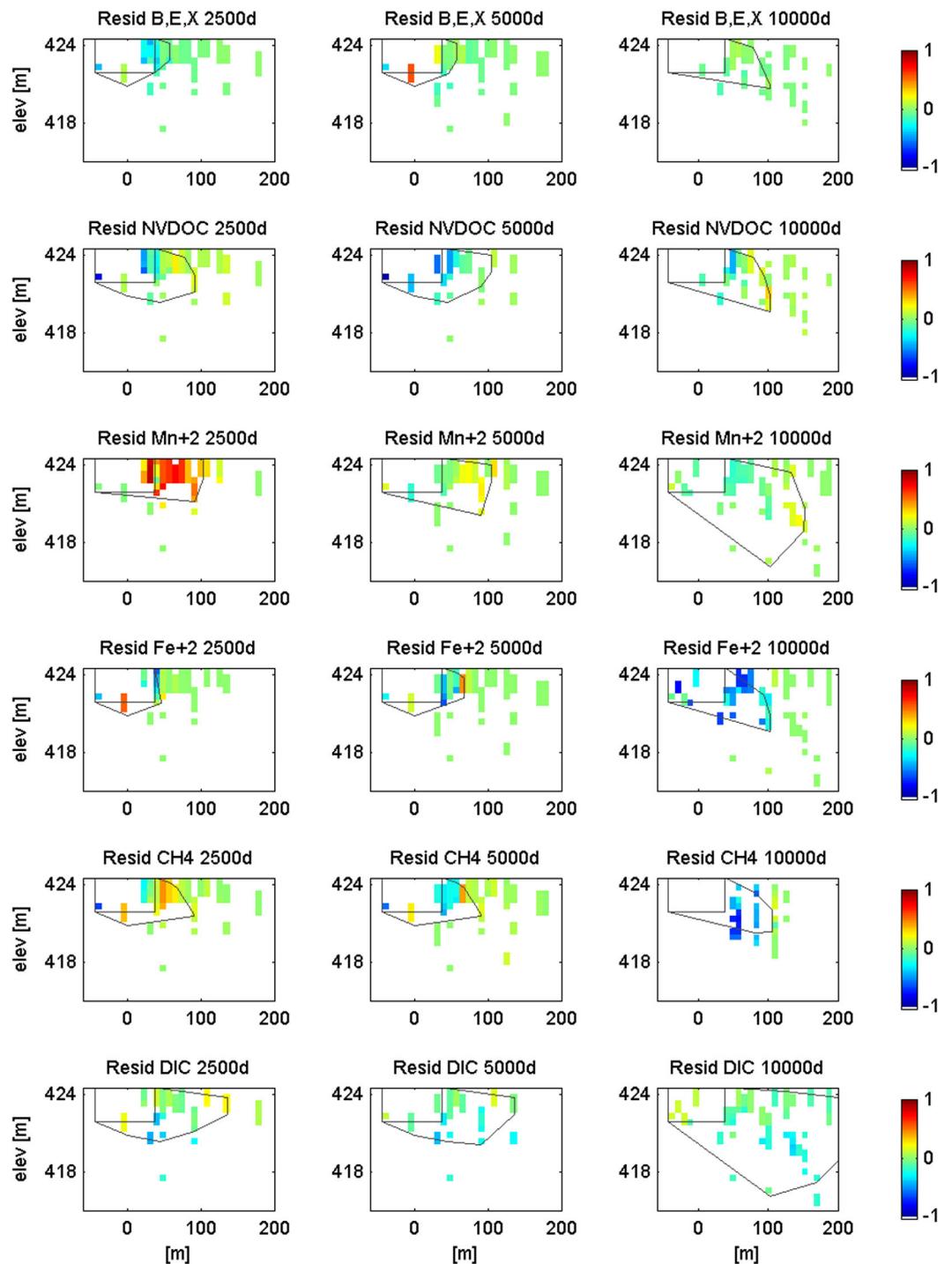
Figure 5. Normalized model residuals (equation (11)) for the six major redox species shown in Figure 4, calculated with corresponding observations at well locations sampled at the three observational periods. Positive (negative) residual signifies observations are higher (lower) that model values. The boxes correspond to the oil body reference rectangle. The polygons outline the observed plume extent for the corresponding component, which are delineated around wells with measurements significantly different than background.

From Figure 5, it can be seen that simulated concentrations of both dissolved BEX and NVDOC are somewhat too high near the oil body at early times (2500 days). Uncertainty in that area may be greater due to subpixel oil and water interactions and sparser data. However, the model does well in capturing later time concentrations and overall temporal changes of dissolved BEX and NVDOC. The distinct characters of these plume changes suggest that properly representing drivers of SWQIs may require accounting for interactions
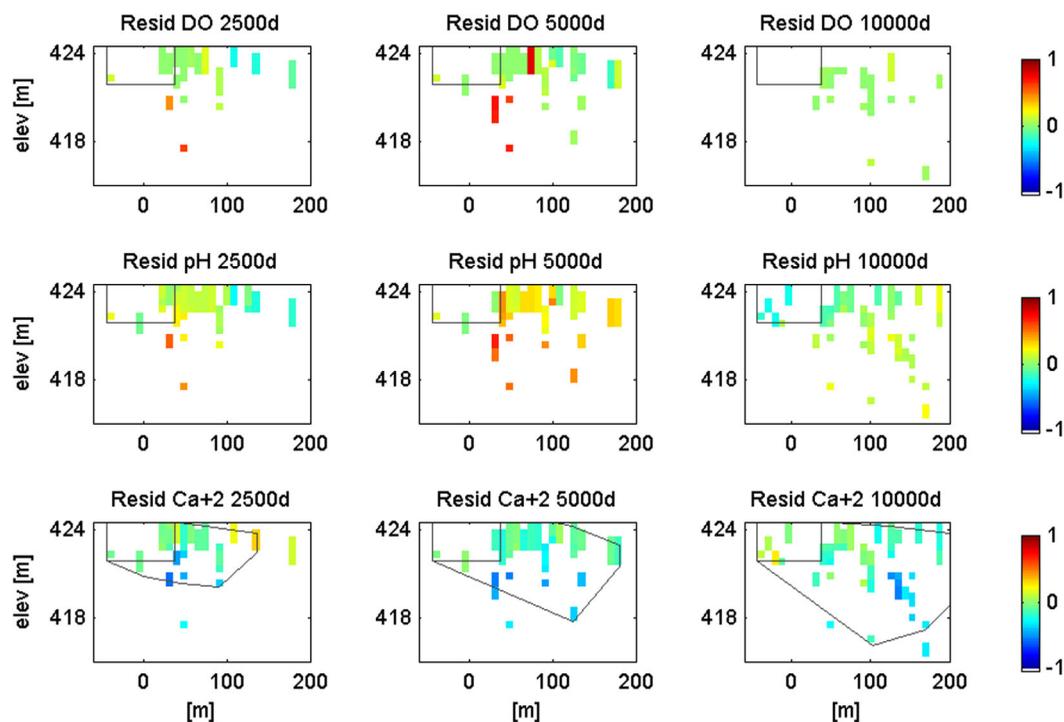
Figure 6. Normalized model residuals (equation (11)) for DO, pH, and Ca^{2+}, calculated with corresponding observations at well locations sampled at the three observational periods. The boxes correspond to the oil body reference rectangle. The polygons outline the observed plume extent for the corresponding component, which are delineated around wells with measurements significantly different than background.

among oil components, such as inhibition behavior. The favorable match at later times in the evolution of this plume indicates that our new inhibition-degradation model for NVDOC production provides a plausible mechanism for the observed shift in organic carbon plume composition.

Observed anaerobic conditions are well simulated (Figure 6), and the model also reproduces the early appearance of Mn^{2+} (Figure 4), which poses a nuisance secondary water quality problem. The Mn mass balance is not well constrained because bioavailable Mn(IV) and sediment-associated Mn(II) are highly uncertain. The model is calibrated to produce Mn^{2+} concentrations around 0.05 mM (Figure 4), consistent with observed Mn^{2+} levels in 1993. The significant discrepancy between 1987 data and simulated Mn^{2+} (Figure 5) is due to very high Mn^{2+} concentrations observed in 1987 but not observed again during later sampling periods. The early elevated levels apparently reflect a transient phenomenon not represented in the model. Later time simulations show an undersimulated Mn^{2+} plume extent. Simulations would likely better match observations if they incorporated more solid phase Mn data and a better sorption model, as further discussed in section 5.4.

The Fe^{2+} plume has over 10 times higher concentrations than Mn^{2+} (Figure SI1). A good match to these data in the simulated plume progression is apparent from the low residuals outside the plume outline at all three times (Figure 5). Following the appearance of dissolved Fe^{2+} by 2500 days, successful simulation of the limited Fe^{2+} plume extent at the end of the simulation at 10,000 days is achieved by representing solid phase immobilization of Fe(II). Negative residuals within the plume outline in Figure 5 at 10,000 days indicate high simulated plume concentrations, which may be due to insufficient sorption model constraints. Overall, the discrepancy between simulated and observed aqueous Fe concentrations is small compared to total reduced Fe concentration when sediment-associated quantities are also considered, and thus the mismatch has little impact on the total electron balance represented.

The early appearance of the CH$_4$ plume and modest plume extent observed at later times also are well matched by the model (Figure 5). Simulating CH$_4$ production by the earliest time period requires low Fe(OH)$_3$ solubility with the partial equilibrium implementation to achieve concomitant Fe reduction and methanogenesis, but this leads to simulation of higher than observed CH$_4$ concentrations at later times
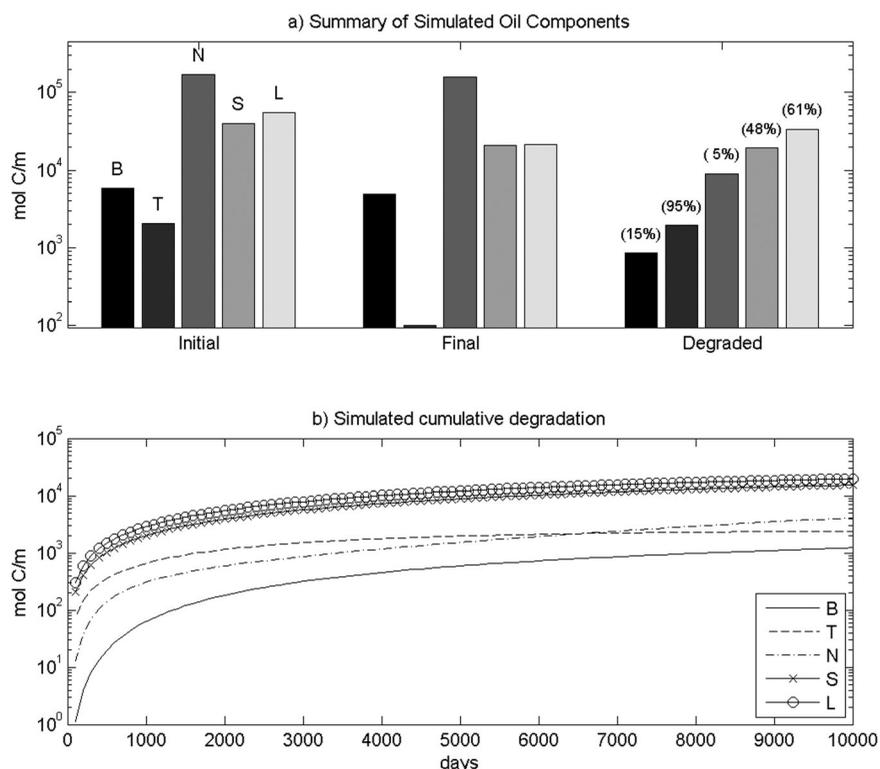
Figure 7. (a) Two-dimensional domain totals (concentrations integrated over 2-D cross-sectional area) for the five oil phase components included in the model (B: BEX, T: toluene, N: preNVDOC, S: short-chain *n*-alkanes, and L: long-chain *n*-alkanes), at the initial time of the spill, at the final simulation time (10,000 days), and for the degraded amount over the simulation period. For each component, the percentage of its initial amount that is degraded at the end of the simulation period is printed in parentheses. (b) For each oil phase component, the total moles of C per aquifer thickness degraded over the simulation.

(Figure 5). The early appearing but moderate concentration CH_4 plume maybe be due subgrid heterogeneity or to kinetic controls on bioavailable Fe mineral dissolution. Given its advantages in facilitating incorporation of secondary, coupled reactions, we favor the partial equilibrium model over a fully kinetic implementation in the model. The partial equilibrium model implementation adequately describes the role of microbially mediated Fe oxide dissolution properties for controlling the Fe plume. Anaerobic methane oxidation coupled to Fe reduction, as proposed by *Amos et al.* [2012], is implicitly represented with our partial equilibrium model, resulting in the limited extent of the CH_4 plume and close correspondence with the Fe^{2+} plume.

Oxidation of organic carbon, through all TEAP pathways, contributes to the significant plume of DIC (Figure 4). High observed DIC concentrations are well simulated, especially near the oil body (Figure 5). Mass balance calculations indicate that matching the observed DIC concentrations requires other sources besides DIC produced from degradation of BTEX coupled to DO, Fe-reduction, and methanogenesis [*Ng et al.*, 2014]. Additional processes incorporated in the model include DIC from the degradation of NVDOC and *n*-alkanes and from dissolution of carbonate minerals. The DIC plume extent appears somewhat oversimulated, from a comparison of full plume results in Figure 4 and the observed plume outlines in Figure 5, but this may be partially due to limited down-gradient data, especially at the two earlier observational periods. The DIC simulation also seems to show the progression of two overlapping plumes originating from the oil body. This detail is due to the distinct oxidation timing of the different oil constituents in the model, especially NVDOC, which degrades only as other compounds become depleted. Fine-resolution concentration variations simulated with the model are difficult to detect from the well samples.

4.2. Oil Phase Simulations

The overall fate of the oil components may be readily compared by integrating their C concentration (moles C/m^3) over the entire 2-D domain (m^2), to arrive at domain totals in moles of C per m. In Figure 7a, the initial

domain totals were specified according to available oil composition data, while the final domain totals were simulated with kinetic parameters to match available oil data at 30 years following the spill (section 3.2). Quantitative measurements of long-chain n-alkanes and precursors to NVDOC are lacking compared to the volatile oil constituents, so their simulations are also calibrated to other aqueous, gas, and solid phase data. Figure 7a shows that of the five modeled oil components, long and short-chain n-alkanes make up the first and second greatest fractions of the degraded oil (52% and 30%), respectively. Most of the degraded carbon from n-alkanes outgases directly as CH_4 or CO_2, with only 5% of the degraded n-alkane carbon forming dissolved CO_2. Of the three other oil components (BEX, preNVDOC, and toluene), which all degrade fully into the aqueous phase, preNVDOC has contributed most of the C degradation (76%). After 10,000 days, preNVDOC makes up the majority (77%) of the remaining oil components, indicating continued importance of NVDOC in driving secondary groundwater impacts at the site. As future concentrations of toluene and n-alkanes drop, decreased competition by their degradation could accelerate the flux of NVDOC from the oil (see equation (6)). However, the preNVDOC category has by far the smallest percent decrease from initial conditions (6%), suggesting that of the possible NVDOC precursors identified by *Thorn and Aiken* [1998], biotransformation may only affect a small fraction.

The total toluene degradation is greater than BEX, even though it makes up a smaller fraction of the initial oil. Figure 7b shows that in terms of moles C, more toluene is degraded within the first half of the simulation period (5000 days) compared to BEX and preNVDOC, indicating that in the early period aqueous conditions were heavily influenced by toluene degradation. At the end of the simulation, 84% of the BEX persists in the oil phase. Properties of the combined BEX component will change in the future, due to its operational treatment as a single model component represented by the properties of benzene. This simplification is computationally convenient, but it is only reasonable as long as benzene makes up the bulk of the BEX dissolution and degradation activity. After most of the benzene is consumed, the remaining members, ethylbenzene and xylenes, will dissolve and degrade at slower rates.

Dissolved organic carbon present in the aquifer at 10,000 days comprises only about 1% of the total oil carbon loss. Dissolved BEX and NVDOC both comprise 11% of their respective losses from their corresponding oil phases. This demonstrates that the dissolved phase of organic carbon is a small transient pool compared to the total degraded organic carbon, and it does not serve as a good indicator of biodegradation activity. These new quantitative results on the Bemidji oil provide insights into the importance of n-alkanes and NVDOC at the site. More generally, they highlight the need to consider multiple electron donors that make up complex organic carbon sources and account for their distinct behavior when evaluating SWQIs from organic carbon biodegradation.

4.3. CH$_4$ and CO$_2$ Outgassing Simulations

Figure 8 shows simulated C gas flux, which includes the contributions from the two model processes: outgassing of CH_4 and CO_2 from the aqueous phase (denoted $CH_4(g)^a$ and $CO_2(g)^a$) and direct outgassing of an undifferentiated mix of CH_4 and CO_2 from n-alkane degradation adjacent to the oil body (denoted $C(g)^d$). It is uncertain how well the seasonally weighted average efflux from *Sihota* [2014], which is based on 2011–2013 data, represents the full 30 year simulation period, but even conservative estimates indicate the gas phase carbon sink to be significant [*Ng et al.*, 2014]. In order to simulate adequate CH_4 and CO_2 to match vadose zone gas data 28 years after the spill, *Molins et al.* [2010] found it necessary to include flux boundary conditions of CH_4 and CO_2 from the water table, which they chose to implement starting 16 years after the spill. Figure 8 compares this study's simulated time series of efflux contributions, integrated over the horizontal interval with efflux detected by *Sihota et al.* [2011], against the portion of the observation from *Sihota* [2014] that is attributed to oil degradation near the water table. At the end of the simulation period, total simulated C efflux from all sources matches well against the observed rate (in gray).

By 30 years after the spill, the model predicts total C efflux to consist overwhelmingly of directly outgassed carbon ($C(g)^d$), which is more than 5 times the total outgassing from the aqueous phase (Figure 8, note different y axis scales). *Amos et al.* [2005] showed decreased N_2 concentrations near the oil body as evidence of outgassing, but N_2 concentrations in 2002–2003 demonstrate that aqueous phase CH_4 production had not reached levels that completely depleted N_2. The observed N_2 is not likely due to advective and diffusive ingress, and so this strongly limits the amount of CH_4 that could be cycled through the aqueous phase.
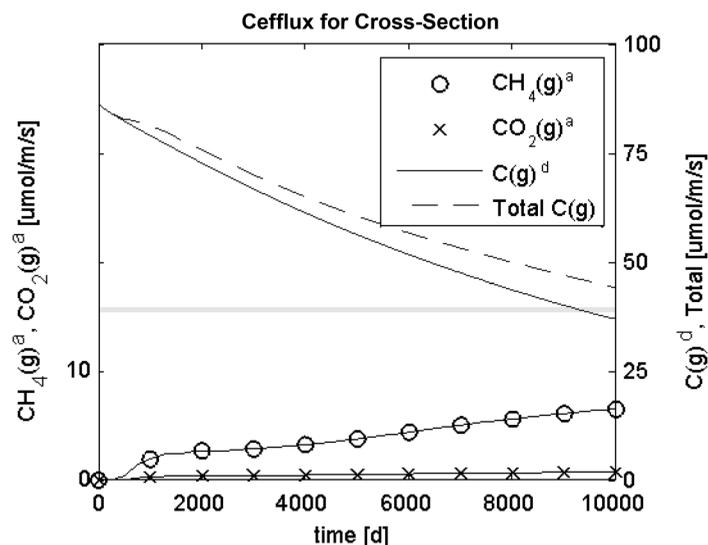
Figure 8. Left y axes: simulated $CH_4(g)^a$ and $CO_2(g)^a$, which are gas effluxes from the aqueous phase. Right y axes: simulated $C(g)^d$, the efflux of undifferentiated C degradation products that are directly outgassed from degradation of n-alkanes; and simulated total $C(g)$, the C efflux from both the aqueous phase and directly outgassed sources. The efflux is integrated over the horizontal interval over which outgassing occurs due to oil biodegradation. The gray line corresponds to the right y axis and indicates the seasonally weighted annual mean measured over 2011–2013 by *Sihota* [2014] that is attributed to oil degradation at and below the water table. The simulated total effluxes are average values at 100 day temporal resolution.

Figure 8 also shows that outgassing from the aqueous phase is mostly all in the form of CH_4, consistent with its much higher volatility compared to CO_2 and with previous vadose zone modeling studies indicating high CH_4 releases relative to CO_2 into the vadose zone [*Molins et al.*, 2010; *Sihota and Mayer*, 2012]. Preferential outgassing of CH_4 maintains low CH_4 to CO_2 concentration ratios, which are observed even where the plume is strongly methanogenic.

Early time simulations show direct outgassing from the water table beginning immediately following the spill and then decreasing with time in response to slowing first-order degradation rates (equation (4)). In contrast, simulated outgassing from the aqueous phase increases with time, as dissolved CH_4 and CO_2 increase in the plume. Of the total outgassing from the aqueous phase over 10,000 days, CH_4 makes up 88%. The model indicates that the recent seasonally weighted average measurements may be lower than early time efflux.

The model formulation with direct outgassing is an approximation for uncharacterized aqueous and gas phase interactions, and it provides a reasonable match to the data. Down-gradient processes not incorporated in the model include bubble entrapment, which *Amos et al.* [2011] demonstrated can limit CH_4 plume extent in the field. Gas bubbles may also enhance CH_4 outgassing directly from the oil body area by lowering the relative permeability to water and limiting the transport of localized water pockets in contact with the degrading oil. Slow horizontal flow and transport in the capillary fringe can allow n-alkane degradation products to outgas with limited interaction with the rest of the plume. Lab-scale experiments have demonstrated discontinuous gas phase mobilization through a DNAPL pool, which generated significant concentrations of the gas compound above the pool [*Mumford et al.*, 2010]. A recent study in a natural asphalt lake reported anaerobic microbes in miniscule water droplets entrapped in oil, providing field evidence for oil degrading apart from the bulk aqueous environment [*Meckenstock et al.*, 2014]. Although the precise mechanism behind our direct outgassing formulation is not clear, its importance in simulations indicates that carbon losses to the gas phase significantly diminish the secondary water quality impacts of oil body degradation.

4.4. Solid Phase Simulations

Figure 9 shows full plume model results for oxidized and reduced solid phases of Mn and Fe, as well as calcite. The rate at which the depleted Mn(IV) mineral front proceeds is directly controlled by the initial bioavailable pyrolusite concentration in the model. There is a lack of conclusive Mn extraction data so the model is calibrated to observed concentrations of dissolved Mn^{2+}. The simulations of pyrolusite (Mn(IV)) and sorbed MnX_2 (Mn(II)) show that the Mn reduction front moves ahead of Fe reduction (Figure 9), as is expected and observed. Simulations indicate that a contributing factor to the observed faster Mn^{2+} transport could be the earlier desorption of Mn compared to Fe, as Mn reduction ceases due to depleted Mn oxides, and exchanged Mn ions are replaced by Fe. This effect is apparent in Figure 9, from the attenuated concentrations of MnX_2 appearing around the oil body area, and spreading down-gradient at later times.
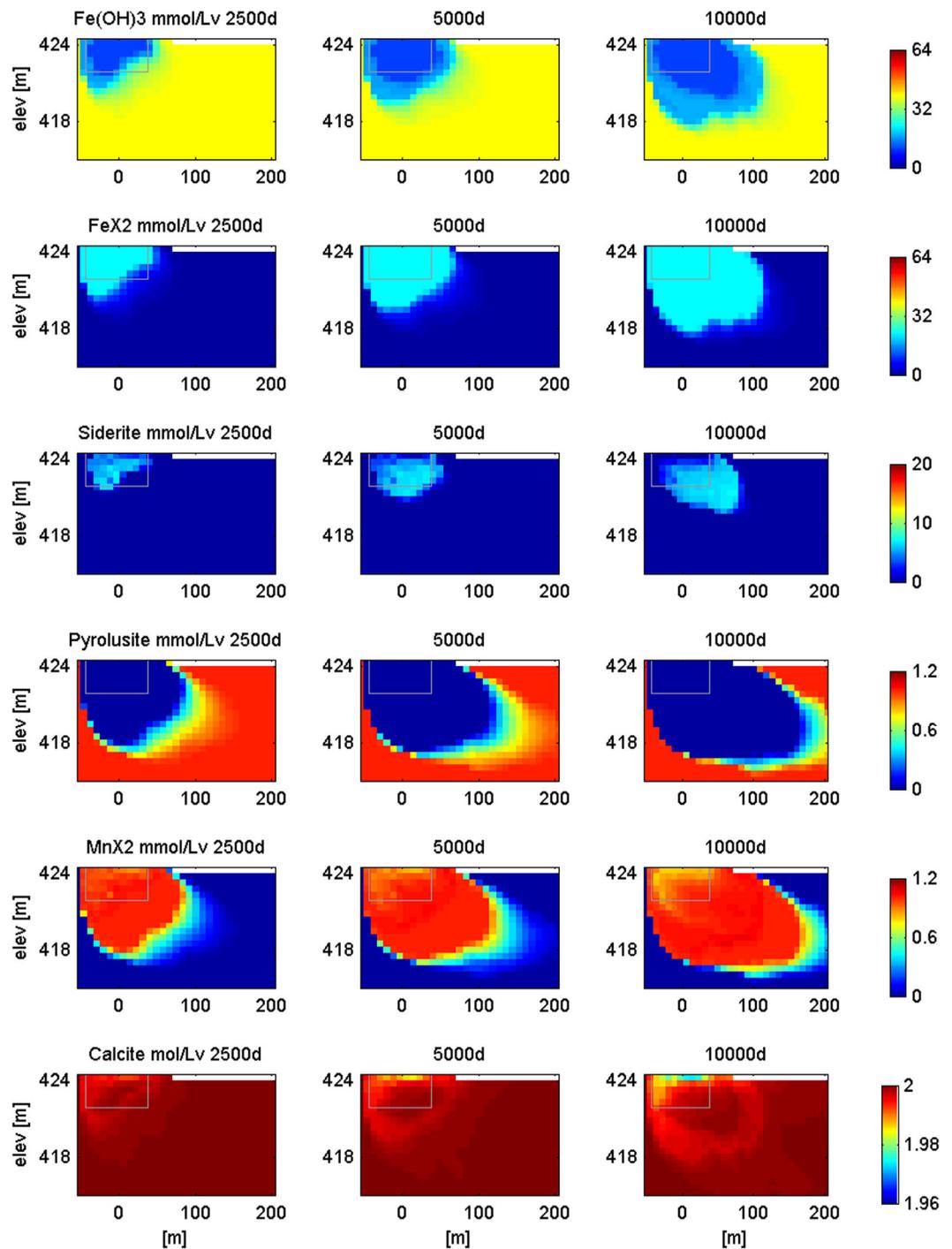
Figure 9. Model simulation results for solid phase components at three times corresponding to the observational time periods. X is the cation exchanger used to represent sorption. $Fe(OH)_3$ represents the Fe(III) electron acceptor, and FeX_2 and siderite ($FeCO_3$) make up the reduced solid phase Fe(II). Pyrolusite (MnO_2) represents the Mn(IV) electron acceptor, and MnX_2 makes up the reduced solid phase Mn(II); no precipitation of rhodochrosite ($MnCO_3$) occurred in the model. Changes in calcite ($CaCO_3$) are caused by pH and aqueous carbonate conditions. The boxes correspond to the oil body reference rectangle.

Figure 10 shows that by 2006–2008, the model reproduces the relatively uniform spatial depletion of Fe(III) that is observed. Comparison of Fe(III) extraction results in Figure 10a with simulated Fe(III) in Figure 10b reveals the model's inability to produce high amounts of Fe(III) over the interval of 80–125 m at 5000 days. *Tuccillo et al.* [1999] attributes the observed above-background concentrations to the
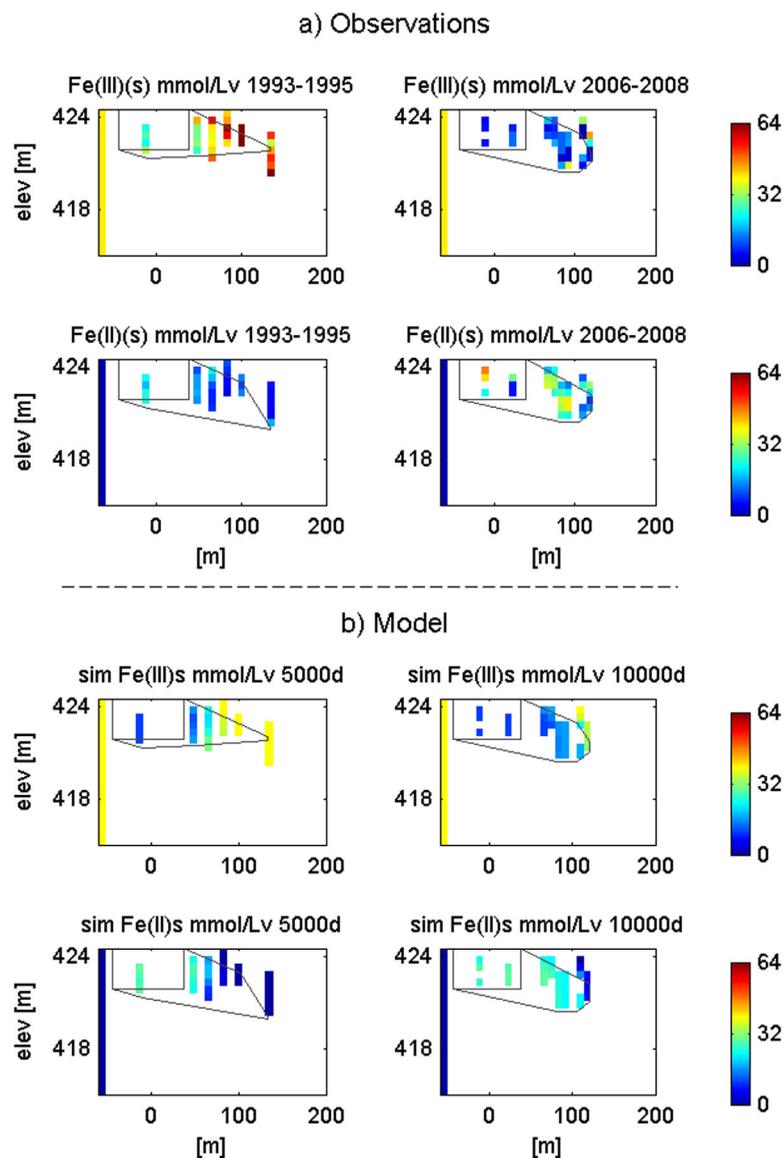
Figure 10. (a) Observed 0.5 M HCl Fe extraction results, available for the latter two observational periods. Results shown for Fe(II) are excess concentrations above background (7.6 mmol/L$_v$). Left-hand stripes indicate background and initial concentrations (0 for no excess Fe(II)). (b) Simulations of solid phase-associated Fe(III) and Fe(II). Fe(III) extraction results are compared against Fe(OH)$_3$ simulations, and excess Fe(II) extraction results are compared against the combined simulations of FeX$_2$ (sorbed Fe(II)) and siderite (precipitated Fe(II)). In both Figures 10a and 10b, the boxes correspond to the oil body reference rectangle, and the polygons outline the observed plume extent for the corresponding component, which are delineated around cores with extraction results significantly different than background. Note that the plume outline in Figure 10b is based on observations and not model results.

reoxidation and precipitation of reduced Fe at the oxidation front. This formation of down-gradient Fe(III) may be due to fine spatial scale availability of DO or to reoxidation by Mn(IV) oxides. In our simulations, DO is uniformly consumed in the plume, and the depleted pyrolusite front moves too far ahead of the Fe^{2+} plume for either of these mechanisms to occur. In the overall long-term redox evolution, the omission of reprecipitated Fe is relatively insignificant, because the reoxidation of Fe simply represents a transient exchange of immobile electron acceptors. Thus, although Fe^{2+} concentrations may be affected during intermediary times, eventual redox conditions and plume growth would not be significantly altered.

Figures 10a and 10b compare observed concentrations of Fe(II) with combined simulations of siderite and sorbed Fe(II), which cannot be differentiated with the extraction method. Importantly, the model

adequately represents the overall amount of Fe reduced, with >99% becoming immobilized on sediments [*Tuccillo et al.*, 1999; *Amos et al.*, 2012; *Ng et al.*, 2014]. Mismatches occur mostly due to fine spatial scale mineral variability not captured by the model, as evidenced by patchy Fe(II) observed among core segments over 2006–2008 (Figure 10). In previous modeling studies, the omission of data constraints on sediment-associated Fe(II) likely led to significant underaccounting of Fe electron acceptors and organic carbon oxidation rates and affected the simulation of other TEAP species.

Simulations indicate that at all locations in the plume, sorbed Fe comprises at least 76% of the total Fe(II), even in the area of greatest siderite precipitation (Figure 9). The importance of sorbed Fe is supported by three lines of evidence with the calibrated simulation. The first is by pH measurements, as further discussed in section 4.5. The second is the observed slow spread of the dissolved Fe^{2+} plume, which is matched in the model through the sharp attenuation of Fe^{2+} at the Fe(II) front, because FeX_2 may form with any amount of Fe^{2+} in solution. In contrast, siderite precipitation requires sufficiently high Fe^{2+} concentrations to meet the saturation threshold, which would allow low Fe^{2+} concentrations to migrate farther down-gradient than observed. Third, simulation results in Figure 9 show siderite precipitating in the plume core after the sorption sites are exhausted. The siderite precipitation continues to take Fe^{2+} out of solution and lowers pH, both of which promote further Fe(III) dissolution and reduction. The ongoing decrease of Fe(III) is consistent with observations (compare observed Fe(III) for 1993–1995 versus 2006–2008 in Figure 10a). The favored form of sorbed over precipitated Fe(II) in the model is consistent with slow kinetic precipitation rates measured for siderite in low temperature anaerobic aquifers [*Jensen et al.*, 2002]. If conditions change in the future to favor remobilization of sorbed Fe, then the dominance of sorbed over precipitated Fe phases may affect the long-term secondary water quality impact of Fe.

The simulation shows equilibrium calcite dissolution occurring near the oil body, likely due to low pH caused by methanogenesis. The Ca^{2+} concentration and plume extent are slightly oversimulated, as shown in Figure 6 (see also Figures SI3–SI4 in the supporting information), which may be due to the omission of Ca sorption in the model. However, the model successfully captures the extensive elevated Ca^{2+} plume, suggesting that calcite dissolution may control the Ca^{2+} plume evolution. Calcite dissolution also releases CO_3^{2-}, which may contribute to the high DIC to CH_4 ratios observed [*Ng et al.*, 2014]. However, the increased alkalinity from calcite dissolution furthers the need for H^+ sources to produce the observed slightly acidic pH levels in the plume. The simulation shows that calcite can be an important influence on secondary water quality impacts because some biodegradation reactions are sensitive to pH or cation balances.

4.5. pH Buffering

Figure 11 shows that the various pH-related model features presented in section 3 allowed for successful simulation of the observed pH, which begins to drop as early as 2500 days and continues to be slightly acidic until the end of the simulation period. Residuals in Figure 6 indicate some difficulty in simulating the 1993 pH values, which were high compared to 1987 and 2009 (see Figure SI4 in the supporting information). However, we capture the overall trend of an early and growing low pH plume, at the typical pH values observed.

Following *Curtis et al.* [1999], our adjusted dissolution log K value for $Fe(OH)_3$ promoted concomitant methanogenesis, which provides an H^+ source and matches the early appearance of the CH_4 plume. However, the observed low pH plume extends far beyond that of CH_4. Either methanotrophy or CH_4 outgassing might help explain the difference in CH_4 and pH plume extents, but aerobic methanotrophy and outgassing of dissolved methane are mostly restricted to areas close to the water table [*Amos et al.*, 2011] and Fe-mediated anaerobic methane oxidation [*Amos et al.*, 2012] would raise pH.

Our sorption model serves as a mechanism for the observed Fe(II) immobilization, and it provides additional H^+ in the same location and time as Fe reduction. *Mayer et al.* [2001] similarly implemented H^+ exchange with cations to simulate pH buffering in a permeable reactive barrier study. Our model results show that sorbed H (HX) concentrations drop as H^+ leaves exchange sites in the location where Fe(III) is depleted and FeX_2 forms (Figure 9). However, results also show that the reservoir of H^+ on surface exchange sites is eventually exhausted. The model also includes dissolution of a fraction of CO_2 produced from *n*-alkane degradation, which forms a weak acid, providing an on-going H^+ source. Significantly, the effects of CO_2 dissolution are restricted to areas close to the oil body, so it cannot supplant collocated pH buffering by desorbed H^+
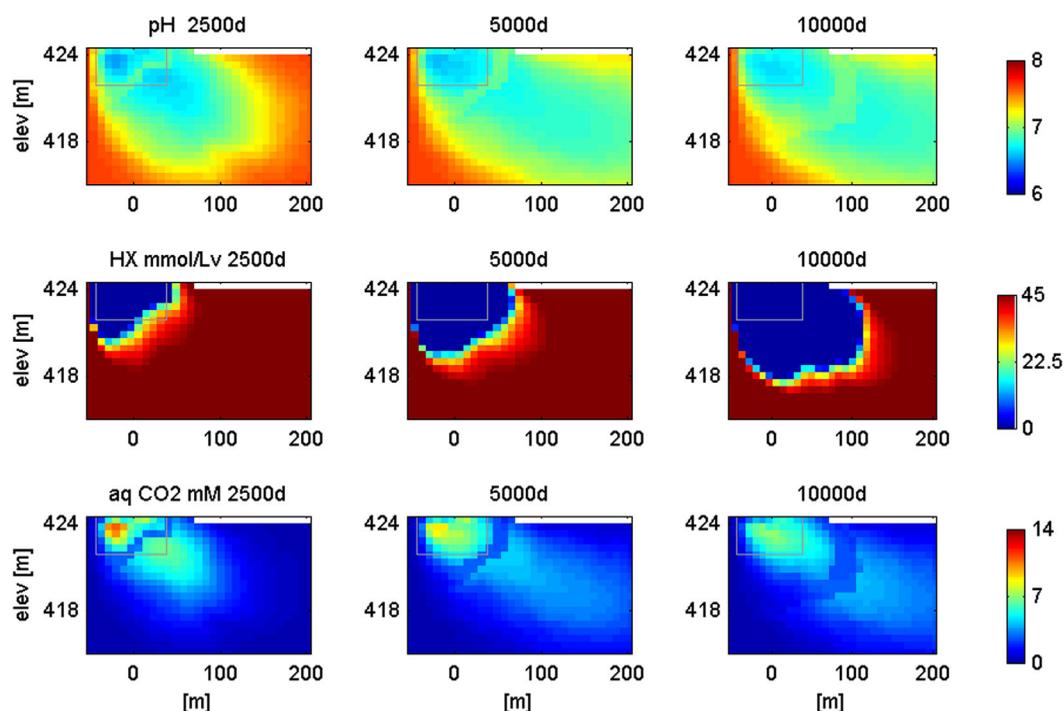
Figure 11. Model simulation results for pH and other components influencing pH at three times corresponding to the observational periods. HX is sorbed H^+, which exchanges with Fe^{2+} and Mn^{2+}. The aqueous form of the weak acid CO_2 also provides a source of low pH. The boxes correspond to the oil body reference rectangle.

in the Fe reduction zone. This is apparent in Figure 11, which shows locations below the oil body reference rectangle with relatively low simulated concentrations of CO_2 but significantly depleted HX. The different H^+ source processes allow simulation of an extensive low pH plume beyond the dissolved CH_4 plume extent. Approximately circumneutral pH perturbations are not generally a water quality concern, but the changes aid the constraint of various processes affecting secondary water quality impacts.

5. Relation to Previous Bemidji Mass Balance Efforts and Recommendations

The modeled time series of CH_4 and Fe^{2+} forms and electron (e^-) balance in Figure 12 summarize the relative contributions of various geochemical processes in controlling SWQIs over the 30 years since the oil spill. The model simulations (Figure 12c) show that the majority (84%) of the electron equivalents of the oil loss at and below the water table is due to direct outgassing produced from n-alkane degradation. However, the carbon mass balance calculated by *Ng et al.* [2014] showed sources from the oil exceeding the observed and inferred sinks by about a factor of 2. To close that gap, adjustments were made in this model for oil constituents that were poorly constrained by data. Long-chain n-alkanes and NVDOC precursors are oil constituents with the least quantitative observations but made up the greatest fractions of C inputs in the mass balance analysis of *Ng et al.* [2014] (68% and 22%). In the model calibration, the fraction of oil composed of long-chain n-alkanes, f_{long} (Table 3) was revised downward from 0.25–0.40 to 0.10, based on newly available data. In addition, total NVDOC degradation was lowered to only 16% of the approximation in *Ng et al.* [2014], which had been based on an estimate with an acknowledged high bias [*Amos et al.*, 2012]. The observed Fe balance presented in *Ng et al.* [2014] was used to constrain the model result of 99% reduced Fe on sediments. The Fe simulations indicate most of the sediment-associated Fe(II) is sorbed, with some precipitated at later times (Figure 12b).

Consistent with previous works that quantified the importance of anaerobic degradation [*Essaid et al.*, 2003; *Amos et al.*, 2012], Figure 12c shows only a small percentage of electron equivalents associated with the total oil loss could be attributed to aerobic degradation (0.09%) (below the scale in Figure 12c) or the dissolved CH_4 pool (0.72%), while a much greater fraction (6% of total) was due to Fe reduction. The model also indicated that CH_4 outgassed from the aqueous phase accounts for as much OC degradation in the
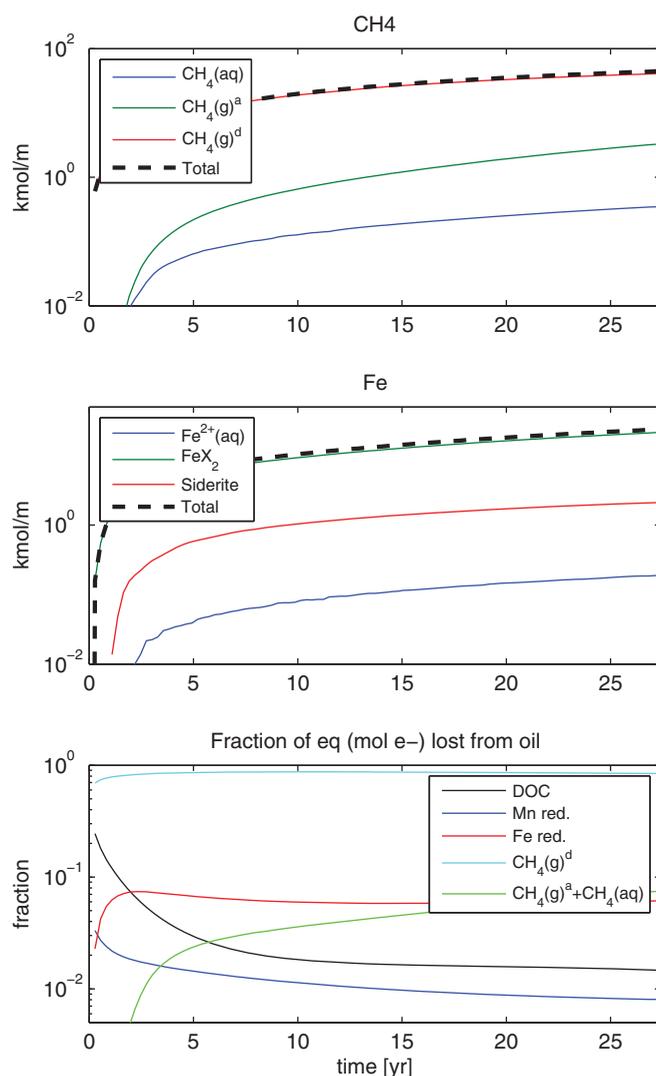
Figure 12. (a) Simulated time series of dissolved CH_4 in the plume ($CH_4(aq)$), outgassed CH_4 from aqueous solution ($CH_4(g)^a$), and directly outgassed CH_4 from n-alkane degradation ($CH_4(g)^d$). (b) Simulated time series of dissolved Fe, sorbed Fe, and siderite. (c) Simulated fraction of e^- balance from various TEAP components and total dissolved organic carbon.

aqueous plume as Fe reduction by the end of the simulation (Figure 12c). This result significantly exceeds the inferred contribution from aqueous outgassed CH_4 in *Ng et al.* [2014], which was less than a tenth of that from Fe reduction. However, temporal dynamics simulated with the model indicate that aqueous phase CH_4 production played a lesser role than Fe reduction in the first 10 years, but may exceed Fe reduction in the future, due to the depletion of bioavailable Fe. The model also suggests that total dissolved organic carbon was larger during the first years following the spill but has decreased with time and comprises little of the lost oil by 30 years (1.5%).

Without the effect of outgassing that bypasses the aqueous phase, simulations would greatly exceed observed concentrations and plume extents of CH_4 and DIC in the aquifer. However, the model also indicates that even with only 5% of CO_2 from degraded n-alkanes entering the aquifer, that amount of dissolved CO_2 is equal to 25% of the total elevated DIC (above background levels) and gaseous CO_2 produced by the end of the simulation. This noteworthy contribution suggests that degradation of the n-alkanes plays a role in driving secondary water quality impacts.

We note that the Bemidji models of *Curtis et al.* [1999] and *Amos* [2006] both incorporated Fe reduction, yet avoided simulating greater than

observed pH values and CH_4 concentrations, without including Fe sorption or other pH-related processes beyond carbonate and hydroxide equilibrium reactions. This was likely achieved due to less total Fe reduction in their simulations, which was possible because those studies did not fully account for all the organic carbon inputs or include the sediment-bound reduced Fe sink. Also, in *Curtis et al.* [1999], the 1-D flow path in equilibrium with atmospheric O_2 likely facilitated CH_4 outgassing and aerobic CH_4 oxidation, both of which help attenuate dissolved CH_4 concentrations.

The lower oil losses in this model, compared to initial inferred values by *Ng et al.* [2014], highlight the need for improved characterization of long-chain n-alkanes and NVDOC at Bemidji, including both their concentrations and their degradation properties. The other poorly constrained component of the model is sorption. Targeted sediment analyses are needed to determine if the simulated dominance of sorbed over precipitated reduced Fe and Mn can be measured. If sorption is dominant, then work is needed to determine the importance of surface complexation versus cation exchange, whether the reaction sites are Fe minerals or clays, and the role of other cations such as Ca^{2+} and Mg^{2+}. The form and mobilization properties of Fe^{2+} and Mn^{2+} have implications for future plume concentrations and other solid phase-related

SWQIs such as arsenic. Further plume monitoring is needed as concentrations change in the future to determine if these metals are remobilized.

6. Summary and Conclusions

This newest Bemidji groundwater modeling study investigates the geochemical processes controlling secondary water quality impacts following a crude oil spill that occurred over 30 years ago. This requires a reactive transport model that can simulate the diverse range of processes that impact the aquifer, including plumes of depleted DO and elevated levels of dissolved organic carbon, Mn^{2+}, Fe^{2+}, CH_4, and inorganic carbon. Drawing on previous modeling studies and on a uniquely extensive and updated set of data at the site, we developed a comprehensive model that includes detailed treatment of multiple organic carbon constituents, mineral phases, sorption processes, and gas phases, in addition to transport processes and a full suite of aqueous system geochemical reactions. The numerical model serves as a powerful tool for evaluating and further elucidating secondary water quality impact processes, including outgassing pathways, pH buffering mechanisms, DIC sources, and immobilization of reduced metals.

By leveraging the most complete organic carbon data set to date from Bemidji, we were able to demonstrate, with the model, the importance of properly characterizing the primary carbon source driving secondary water quality impacts. Supported by observations, we formulate new carbon input mechanisms in the model to account for not only the more traditionally considered BTEX mix, but also the significant pools of n-alkanes and other nonvolatile organic carbon compounds. This includes the direct production and outgassing of degradation products from n-alkanes, constrained by observed surface efflux of CO_2. We also propose a new dissolution model for the formation of NVDOC from their oil phase precursors, which incorporates noncompetitive inhibition by simpler and presumably more easily degraded oil compounds. We find that plumes of secondary water quality species, such as Fe^{2+}, Mn^{2+}, and CH_4, are likely to persist into the future, as the organic carbon source shifts to remaining oil components. However, secondary plumes of dissolved CH_4 are significantly attenuated by outgassing, much of which appears to occur with little aqueous phase interaction.

Another major geochemical component further elucidated with the model is the role of solid phase Fe. Most previous Bemidji models have either overlooked or simplified representations of sediment-associated Fe(II), which makes up 99% of the total reduced Fe. Immobilization on sediments strongly limits the secondary plume growth of Fe and other reduced metals. The model results suggest that much of the reduced Fe sorbs on sediments, a process not explicitly investigated in detail in previous Bemidji studies. The model also showed that precipitated siderite serves as an additional Fe sink that could facilitate continued and gradual depletion of ferric oxide minerals. The form of reduced Fe on sediments may affect its stability, which controls the likelihood of remobilization and future plume persistence.

Although a relatively minor secondary water quality concern, pH is both a strong indicator and driver of coupled redox reactions and thus plays a significant role in constraining the model formulation. To counter the high consumption of H^+ by Fe-mediated degradation, the model framework relies on three mechanisms: (1) concomitant iron reduction and methanogenesis; (2) metal sorption with H^+ exchange; and (3) dissolution of CO_2 (a weak acid) from degradation of n-alkanes. Simulations demonstrate the combined effect of the multiple pH buffers, with sorption providing a collocated H^+ source with Fe reduction and methanogenesis, together with CO_2 dissolution maintaining a sustained pH plume.

Many of the newly introduced model pathways serve multiple purposes for matching observations of critical secondary aqueous species. In addition to providing for the observed low pH plume, simultaneous TEAPs also help produce the observed early onset of elevated CH_4, sorption provides a mechanism for Fe^{2+} plume attenuation, and CO_2 dissolution contributes toward closing the observed carbon balance. This demonstrates the strongly coupled nature of the geochemical components controlling secondary water quality impacts. With this extensive and tightly interwoven network, a comprehensive reactive transport model is necessary for resolving the full spatiotemporal and geochemical relationships.

This study proposes a model that is consistent with multiple data sets at Bemidji, yet challenges remain in simulating early but moderated levels of dissolved CH_4, developing a well-calibrated sorption model, quantifying sediment-associated Mn, and constraining nonvolatile organic carbon concentrations and decay

rates. New sediment and oil analyses are needed to clarify these processes or offer alternative conceptualizations of the data. Although calibrated to conditions at the Bemidji oil spill site, the model demonstrates the importance of characterizing primary electron donor components, mineral processes, solid and gas phase plume attenuation mechanisms, and pH effects when investigating secondary water quality impacts at anaerobic biodegradation sites.

References

AFCEE (Air Force Center for Environmental Excellence) (2004), *Principles and Practices of Enhanced Anaerobic Bioremediation of Chlorinated Solvents*, San Antonio, Tex.

Amos, R. T. (2006), Integrated investigation of natural attenuation in a petroleum hydrocarbon contaminated aquifer, PhD thesis, Univ. of B. C., Dep. of Earth and Ocean Sci., Vancouver, Canada.

Amos, R. T., and K. U. Mayer (2006), Investigating the role of gas bubble formation and entrapment in contaminated aquifers–Reactive transport modeling, *J. Contam. Hydrol.*, *87*(1–2), 123–154.

Amos, R. T., K. U. Mayer, B. A. Bekins, G. N. Delin, and R. L. Williams (2005), Use of dissolved and vapor-phase gases to investigate methanogenic degradation of petroleum hydrocarbon contamination in the subsurface, *Water Resour. Res.*, *41*, W02001, doi:10.1029/2004WR003433.

Amos, R. T., B. A. Bekins, G. N. Delin, I. M. Cozzarelli, D. W. Blowes, and J. D. Kirshtein (2011), Methane oxidation in a crude oil contaminated aquifer—Delineation of aerobic reactions at the plume fringes, *J. Contam. Hydrol.*, *125*(1-4), 13–25, doi:10.1016/j.jconhyd.2011.04.003.

Amos, R. T., B. A. Bekins, I. M. Cozzarelli, M. A. Voytek, J. D. Kirshtein, E. J. P. Jones, and D. W. Blowes (2012), Evidence for iron-mediated anaerobic methane oxidation in a crude oil-contaminated aquifer, *Geobiology*, *10*(6), 506–517, doi:10.1111/j.1472-4669.2012.00341.x.

Anderson, R. T., and D. R. Lovley (1999), Naphthalene and benzene degradation under Fe(III)-reducing conditions in petroleum-contaminated aquifers, *Bioremediation J.*, *3*(2), 121–135, doi:10.1080/10889869991219271.

Aronson, D., and P. H. Howard (1997), Anaerobic biodegradation of organic chemicals in groundwater: A summary of field and laboratory studies, *Rep. SRC TR-97–0223F*, Syracuse Res. Corp., North Syracuse, N. Y.

Atekwana, E. A., F. M. Mewafy, G. A. Aal, D. D. Werkema, Jr., A. Revil, and L. D. Slater (2014), High-resolution magnetic susceptibility measurements for investigating magnetic mineral formation during microbial mediated iron reduction, *J. Geophys. Res. Biogeosci.*, *119*(1), 80–94.

Baedecker, M. J., I. M. Cozzarelli, J. R. Evans, and P. P. Hearn (1992), Authigenic mineral formation in aquifers rich in organic material, in *Low Temperature Environments, Water-Rock Interaction—Proceedings of the 7th International Symposium on Water-Rock Interaction—WRI-7*, vol. 1, edited by Y. K. Kharaka and A. S. Maest, pp. 257–261, A. A. Balkema, Rotterdam, Netherlands.

Baedecker, M. J., I. M. Cozzarelli, D. I. Siegel, P. C. Bennett, and R. P. Eganhouse (1993), Crude oil in a shallow sand and gravel aquifer–III. Biogeochemical reactions and mass balance modeling in anoxic ground water, *Appl. Geochem.*, *8*(6), 569–586.

Baedecker, M. J., R. P. Eganhouse, B. A. Bekins, and G. N. Delin (2011), Loss of volatile hydrocarbons from an LNAPL oil source, *J. Contam. Hydrol.*, *126*(3-4), 140–152, doi:10.1016/j.jconhyd.2011.06.006.

Barry, D. A., H. Prommer, C. T. Miller, P. Engesgaard, A. Brun, and C. Zheng (2002), Modelling the fate of oxidisable organic contaminants in groundwater, *Adv. Water Resour.*, *25*(8), 945–983.

Bekins, B. A., F. D. Hostettler, W. N. Herkelrath, G. N. Delin, E. Warren, and H. I. Essaid (2005), Progression of methanogenic degradation of crude oil in the subsurface, *Environ. Geosci.*, *12*(2), 139–152, doi:10.1306/eg.11160404036.

Bennett, P. C., D. I. Siegel, M. J. Baedecker, and M. F. Hult (1993), Crude oil in a shallow sand and gravel aquifer–I. Hydrogeology and inorganic geochemistry, *Appl. Geochem.*, *8*(6), 529–549.

Borden, R. C. (2007), Effective distribution of emulsified edible oil for enhanced anaerobic bioremediation. *J. Contam. Hydrol. 94*, 1–12.

Brun, A., and P. Engesgaard (2002), Modelling of transport and biogeochemical processes in pollution plumes: Literature review and model development, *J. Hydrol.*, *256*(3), 211–227.

Brun, A., P. Engesgaard, T. H. Christensen, and D. Rosbjerg (2002), Modelling of transport and biogeochemical processes in pollution plumes: Vejen landfill, Denmark, *J. Hydrol.*, *256*(3), 228–247.

Callaghan, A. V. (2013), Enzymes involved in the anaerobic oxidation of n-alkanes: From methane to long-chain paraffins, *Frontiers Microbiol.*, *4*(89), 1–9, doi:10.3389/fmicb.2013.00089.

Chaplin, B. P., G. N. Delin, R. J. Baker, and M. A. Lahvis (2002), Long-term evolution of biodegradation and volatilization rates in a crude oil-contaminated aquifer, *Bioremediation J.*, *6*(3), 237–255.

Charlet, L., and C. Tournassat (2005), Fe (II)-Na (I)-Ca (II) cation exchange on montmorillonite in chloride medium: Evidence for preferential clay adsorption of chloride–metal ion pairs in seawater, *Aquat. Geochem.*, *11*(2), 115–137.

Cox, E. E. (2009), Development of in situ bioremediation technologies for perchlorate, in *In Situ Bioremediation of Perchlorate in Groundwater*, edited by H. F. Stroo and C. H. Ward, pp. 15–27, Springer, N. Y.

Cozzarelli, I. M., R. P. Eganhouse, and M. J. Baedecker (1990), Transformation of monoaromatic hydrocarbons to organic acids in anoxic ground-water environment, *Environ. Geol. Water Sci.*, *16*(2), 135–141.

Cozzarelli, I. M., B. A. Bekins, M. J. Baedecker, G. R. Aiken, R. P. Eganhouse, and M. E. Tuccillo (2001), Progression of natural attenuation processes at a crude-oil spill site—I, Geochemical evolution of the plume, *J. Contam. Hydrol.*, *53*(3-4), 369–385, doi:10.1016/S01697722(01)00174-7.

Cozzarelli, I. M., B. A. Bekins, R. P. Eganhouse, E. Warren, and H. I. Essaid (2010), In situ measurements of volatile aromatic hydrocarbon biodegradation rates in groundwater, *J. Contam. Hydrol.*, *111*(1-4), 48–64, doi:10.1016/j.jconhyd.2009.12.001.

Curtis, G. P. (2003), Comparison of approaches for simulating reactive solute transport involving organic degradation reactions by multiple terminal electron acceptors, *Comput. Geosci.*, *29*(3), 319–329, doi:10.1016/S0098-3004(03)00008-6.

Curtis, G. P., I. M. Cozzarelli, M. J. Baedecker, and B. A. Bekins (1999), Coupled biogeochemical modeling of ground water contamination at the Bemidji, Minnesota, crude oil spill site, in *U.S. Geological Survey Toxic Substances Hydrology Program-Proceedings of the Technical Meeting, Charleston, South Carolina, March 8–12, 1999—Volume 3 of 3—Subsurface Contamination from Point Sources, U.S. Geol. Surv. Water Resour. Invest. Rep. 99-4018C*, edited by D. W. Morganwalp and H. T. Buxton, pp. 153–158, U.S. Geol. Surv., West Trenton, NJ.

D'Affonseca, F. M., H. Prommer, M. Finkel, P. Blum, and P. Grathwohl (2011), Modeling the long-term and transient evolution of biogeochemical and isotopic signatures in coal tar–contaminated aquifers, *Water Resour. Res.*, *47*, W05518, doi:10.1029/2010WR009108.

Davis, J. A., and D. B. Kent (1990), Surface complexation modeling in aqueous geochemistry, *Rev. Mineral.*, *23*, 177–260.

Dillard, L. A., H. I. Essaid, and W. N. Herkelrath (1997), Multiphase flow modeling of a crude-oil spill site with a bimodal permeability distribution, *Water Resour. Res.*, *33*(7), 1617–1632, doi:10.1029/97WR00857.

Eganhouse, R. P., M. J. Baedecker, I. M. Cozzarelli, G. R. Aiken, K. A. Thorn, and T. F. Dorsey (1993), Crude oil in a shallow sand and gravel aquifer–II. Organic geochemistry, *Appl. Geochem.*, *8*(6), 551–567.

Essaid, H. I., W. N. Herkelrath, and K. M. Hess (1993), Simulation of fluid distributions observed at a crude-oil spill site incorporating hysteresis, oil entrapment, and spatial variability of hydraulic-properties, *Water Resour. Res.*, *29*(6), 1753–1770.

Essaid, H. I., B. A. Bekins, E. M. Godsy, E. Warren, M. J. Baedecker, and I. M. Cozzarelli (1995), Simulation of aerobic and anaerobic biodegradation processes at a crude oil spill site, *Water Resour. Res.*, *31*(12), 3309–3327, doi:10.1029/95WR02567.

Essaid, H. I., I. M. Cozzarelli, R. P. Eganhouse, W. N. Herkelrath, B. A. Bekins, and G. N. Delin (2003), Inverse modeling of BTEX dissolution and biodegradation at the Bemidji, MN crude-oil spill site, *J. Contam. Hydrol.*, *67*(1-4), 269–299, doi:10.1016/S0169-7722(03)00034-2.

Essaid, H. I., B. A. Bekins, W. N. Herkelrath, and G. N. Delin (2011), Crude oil at the Bemidji Site—25 years of monitoring, modeling, and understanding, *Ground Water*, *49*(5), 706–726, doi:10.1111/j.1745–6584.2009.00654.x.

Fletcher, P., and G. Sposito (1989), Chemical modeling of clay/electrolyte interactions of montmorillonite, *Clay Miner.*, *24*(2), 375–391.

Harbaugh, A. W. (2005), MODFLOW-2005, the U.S. Geological Survey modular ground-water model – the Ground-Water Flow Process: U.S. Geological Survey Techniques and Methods, 6–A16.

Hatzinger, P. B. (2005), Perchlorate biodegradation for water treatment, *Environ. Sci. Technol.*, *39*(11), 239A–247A.

Herkelrath, W. N. (1999), Impacts of remediation at the Bemidji oil spill site, in *U.S. Geological Survey Toxic Substances Hydrology Program-Proceedings of the Technical Meeting, Charleston, South Carolina, March 8-12, 1999— Volume 3 — Subsurface Contamination from Point Sources, U.S. Geological Survey Water-Resources Investigations Report 99-4018C*, edited by D.W. Morganwalp and H.T. Buxton, pp. 195–200, U.S. Geol. Surv., West Trenton, N. J.

Hiemstra, T., and W. H. van Riemsdijk (2007), Adsorption and surface oxidation of Fe(II) on metal (hydr)oxides, *Geochim. Cosmochim. Acta*, *71*, 5913–5933, doi:10.1016/j.gca.2007.09.030.

Hostettler, F. D., and K. A. Kvenvolden (2002), Alkylcyclohexanes in environmental geochemistry, *Environ. Forensics*, *3*(3-4), 293–301, doi:10.1080/713848390.

Hostettler, F. D.,Y. Wang, Y. Huang, W. Cao, B. A. Bekins, C. E. Rostad, C. F. Kulpa, and A. Laursen (2007), Forensic fingerprinting of oil-spill hydrocarbons in a methanogenic environment-Mandan, ND and Bemidji, *MN, Environ. Forensic*, *8*(1), 139–153, doi:10.1080/15275920601180685.

Hunter, K. S., Y. Wang, and P. Van Cappellen (1998), Kinetic modeling of microbially-driven redox chemistry of subsurface environments: Coupling transport, microbial metabolism and geochemistry, *J. Hydrol.*, *209*(1), 53–80.

Islam, J., N. Singhal, and M. O'Sullivan (2001), Modeling biogeochemical processes in leachate-contaminated soils: A review, *Transp. Porous Media*, *43*(3), 407–440.

Jakobsen, R., and D. Postma (1999), Redox zoning, rates of sulfate reduction and interactions with Fe-reduction and methanogenesis in a shallow sandy aquifer, Rømø, Denmark, *Geochim. Cosmochim. Acta*, *63*(1), 137–151.

Jensen, D. L., J. K. Boddum, J. C. Tjell, and T. H. Christensen (2002), The solubility of rhodochrosite (MnCO 3) and siderite (FeCO 3) in anaerobic aquatic environments, *Appl. Geochem.*, *17*(4), 503–511.

Jeon, B. H., B. A. Dempsey, and W. D. Burgos (2003), Kinetics and mechanisms for reactions of Fe (II) with iron (III) oxides, *Environ. Sci. Technol.*, *37*(15), 3309–3315.

Li, L., C. I. Steefel, M. B. Kowalsky, A. Englert, and S. S. Hubbard (2010), Effects of physical and geochemical heterogeneities on mineral transformation and biomass accumulation during biostimulation experiments at Rifle, Colorado, *J. Contam. Hydrol.*, *112*(1), 45–63.

Liger, E., L. Charlet, and P. Van Cappellen (1999), Surface catalysis of uranium(VI) reduction by iron(II), *Geochim. Cosmochim. Acta*, *63*, 2939–2955.

Lloyd, J. R., and D. R. Lovley (2001), Microbial detoxification of metals and radionuclides, *Curr. Opin. Biotechnol.*, *12*(3), 248–253.

Lønborg, M. J., P. Engesgaard, P. L. Bjerg, and D. Rosbjerg (2006), A steady state redox zone approach for modeling the transport and degradation of xenobiotic organic compounds from a landfill site, *J. Contam. Hydrol.*, *87* (3-4), 191–210, doi:10.1016/j.jconhyd.2006.05.004.

Martin, S. T. (2005), Precipitation and dissolution of iron and manganese oxides, in *Environmental Catalysis*, edited by V. H. Grassian, pp. 61–82, CRC Press, Boca Raton, Fla.

Mayer, K. U., S. G. Benner, E. O. Frind, S. F. Thornton, and D. N. Lerner (2001), Reactive transport modeling of processes controlling the distribution and natural attenuation of phenolic compounds in a deep sandstone aquifer, *J. Contam. Hydrol.*, *53*(3), 341–368.

Mayer, K. U., E. O. Frind, and D. W. Blowes (2002), Multicomponent reactive transport modeling in variably saturated porous media using a generalized formulation for kinetically controlled reactions, *Water Resour. Res.*, *38*(9), 1174–1194.

McNab, W. W., Jr., and T. N. Narasimhan (1995), Reactive transport of petroleum hydrocarbon constituents in a shallow aquifer: Modeling geochemical interactions between organic and inorganic species, *Water Resour. Res.*, *31*(8), 2027–2033.

Meckenstock, R. U., et al. (2014), Water droplets in oil are microhabitats for microbial life, *Science*, *345*(6197), 673–676.

Miles, B., A. Peter, and G. Teutsch (2008), Multicomponent simulations of contrasting redox environments at an LNAPL site, *Groundwater*, *46*(5), 727–742, doi:10.1111/j.1745-6584.2008.00457.x.

Molins, S., K. U. Mayer, R. T. Amos, and B. A. Bekins (2010), Vadose zone attenuation of organic compounds at a crude oil spill site—Interactions between biogeochemical reactions and multicomponent gas transport, *J. Contam. Hydrol.*, *112*(1), 15–29.

Morse, J. W., and R. S. Arvidson (2002), The dissolution kinetics of major sedimentary carbonate minerals, *Earth Sci. Rev.*, *58*(1), 51–84.

Mumford, K. G., J. E. Smith, and S. E. Dickson (2010), The effect of spontaneous gas expansion and mobilization on the aqueous-phase concentrations above a dense non-aqueous phase liquid pool, *Adv. Water Resour.*, *33*(4), 504–513.

Nicol, J. P., W. R. Wise, F. J. Molz, and L. D. Benefield (1994), Modeling biodegradation of residual petroleum in a saturated porous column, *Water Resour. Res.*, *30*(12), 3313–3325.

Ng, G.-H. C., B. A. Bekins, I. M. Cozzarelli, M. J. Baedecker, P. C. Bennett, and R. T. Amos (2014), A mass balance approach to investigating geochemical controls on secondary water quality impacts at a crude oil spill site near Bemidji, MN, *J. Contam. Hydrol.*, *164*, 1–15, doi:10.1016/j.jconhyd.2014.04.006.

Parkhurst, D. L., and C. A. J. Appelo (1999), User's guide to PHREEQC: A computer program for speciation, reaction-path, ID-transport, and inverse geochemical calculations, *U.S. Geol. Surv. Water Resour. Invest. Rep.*, 99–4259, 312 p.

Pedersen, H. D., D. Postma, R. Jakobsen, and O. Larsen (2005), Fast transformation of iron oxyhydroxides by the catalytic action of aqueous Fe (II), *Geochim. Cosmochim. Acta*, *69*(16), 3967–3977.

Prommer, H., G. B. Davis, and D. A. Barry (1999a), Geochemical changes during biodegradation of petroleum hydrocarbons: Field investigations and biogeochemical modelling, *Org. Geochem.*, *30*(6), 423–435.

Prommer, H., D. A. Barry, and G. B. Davis (1999b), A one-dimensional reactive multi-component transport model for biodegradation of petroleum hydrocarbons in groundwater, *Environ. Model. Software*, *14*(2/3), 213–223.

Prommer, H., D. A. Barry, and C. Zheng (2003), MODFLOW/MT3DMS-based reactive multicomponent transport modeling, *Ground Water*, *41*, 247–257, doi:10.1111/j.1745–6584.2003.tb02588.x.

Revesz, K., T. B. Coplen, M. J. Baedecker, P. D. Glynn, and M. F. Hult (1995), Methane production and consumption monitored by stable H and C isotope ratios at a crude oil spill site, Bemidji, *Minnesota, Appl. Geochem.*, *10*(5), 505–516, doi:10.1016/0883-2927(95)00021-6.

Rodgers, J. D., and N. J. Bunce (2001), Treatment methods for the remediation of nitroaromatic explosives, *Water Res.*, *35*(9), 2101–2111.

Siddique, T., R. Gupta, P. M. Fedorak, M. D. MacKinnon, and J. M. Foght (2008), A first approximation kinetic model to predict methane generation from an oil sands tailings settling basin, *Chemosphere*, *72*, 1573–1580, doi:10.1016/j.chemosphere.2008.04.036.

Sihota, N. J. (2014), Novel approaches for quantifying source zone natural attenuation of fossil and alternative fuels, PhD thesis, Dep. of Geol. Sci., Univ. of B. C., Vancouver, Canada.

Sihota, N. J., and K. U. Mayer (2012), Characterizing vadose zone hydrocarbon biodegradation using carbon dioxide effluxes, isotopes, and reactive transport modeling *Vadose Zone J.*, *11*(4), doi:10.2136/vzj2011.0204.

Sihota, N. J., O. Singurindy, and K. U. Mayer (2011), CO_2-efflux measurements for evaluating source zone natural attenuation rates in a petroleum hydrocarbon contaminated aquifer, *Environ. Sci. Technol.*, *45*(2), 482–488, doi:10.1021/es1032585.

Singhal, N., and J. Islam (2008), One-dimensional model for biogeochemical interactions and permeability reduction in soils during leachate permeation, *J. Contam. Hydrol.*, *96*(1), 32–47.

Steefel, C. I., D. J. DePaolo, and P. C. Lichtner (2005), Reactive transport modeling: An essential tool and a new research approach for the Earth sciences, *Earth Planet. Sci. Lett.*, *240*(3), 539–558.

Stroo, H. F., and C. H. Ward (2010), Future directions and research needs for chlorinated solvent plumes, in *In Situ Remediation of Chlorinated Solvent Plumes*, edited by H. F. Stroo and C. H. Ward, pp. 699–725, Springer, N. Y.

Suarez, M. P., and H. S. Rifai (1999), Biodegradation rates for fuel hydrocarbons and chlorinated solvents in groundwater, *Bioremediation J.*, *3*(4), 337–362.

Thorn, K. A., and G. R. Aiken (1998), Biodegradation of crude oil into nonvolatile organic acids in a contaminated aquifer near Bemidji, Minnesota, *Org. Geochem.*, *29*(4), 909–931.

Thullner, M., P. Regnier, and P. Van Cappellen (2007), Modeling microbially induced carbon degradation in redox-stratified subsurface environments: Concepts and open questions, *Geomicrobiol. J.*, *24*(3-4), 139–155.

Tuccillo, M. E., I. M. Cozzarelli, and J. S. Herman (1999), Iron reduction in the sediments of a hydrocarbon-contaminated aquifer, *Appl. Geochem.*, *14*(5), 655–667.

van Breukelen, B. M., J. Griffioen, W. F. Röling, and H. W. van Verseveld (2004), Reactive transport modelling of biogeochemical processes and carbon isotope geochemistry inside a landfill leachate plume, *J. Contam. Hydrol.*, *70*(3), 249–269.

Vencelides, Z., O. Sracek, and H. Prommer (2007), Modelling of iron cycling and its impact on the electron balance at a petroleum hydrocarbon contaminated site in Hnevice, Czech Republic, *J. Contam. Hydrol.*, *89*(3), 270–294.

Zachara, J. M., R. K. Kukkadapu, P. L. Gassman, A. Dohnalkova, J. K. Fredrickson, and T. Anderson (2004), Biogeochemical transformation of Fe minerals in a petroleum-contaminated aquifer, *Geochim. Cosmochim. Acta*, *68*(8), 1791–1805, doi:10.1016/j.gca.2003.09.022.

Zengler, K., H. H. Richnow, R. Rosselló-Mora, W. Michaelis, and F. Widdel (1999), Methane formation from long-chain alkanes by anaerobic microorganisms, *Nature*, *401*(6750), 266–269.

Zheng, C., and P. P. Wang (1999), MT3DMS: A modular three-dimensional multispecies model for simulation of advection, dispersion and chemical reactions of contaminants in groundwater systems: Documentation and user's guide, *Contract Rep. SERDP-99-1*, U.S. Army Eng. Res. and Dev. Cent., Vicksburg, Miss.